



uOttawa

L'Université canadienne
Canada's university

FACULTÉ DES ÉTUDES SUPÉRIEURES
ET POSTDOCTORALES



uOttawa

l'Université canadienne
Canada's university

FACULTY OF GRADUATE AND
POSTDOCTORAL STUDIES

Ou Chen

AUTEUR DE LA THÈSE / AUTHOR OF THESIS

M.Sc. (Physics)

GRADE / DEGREE

Department of Physics

FACULTÉ, ÉCOLE, DÉPARTEMENT / FACULTY, SCHOOL, DEPARTMENT

Development of Offset Locking Based Distributed Sensor and Study of Polarization Effects in Optical
Fibers

TITRE DE LA THÈSE / TITLE OF THESIS

X. Rao

DIRECTEUR (DIRECTRICE) DE LA THÈSE / THESIS SUPERVISOR

CO-DIRECTEUR (CO-DIRECTRICE) DE LA THÈSE / THESIS CO-SUPERVISOR

EXAMINATEURS (EXAMINATRICES) DE LA THÈSE / THESIS EXAMINERS

J. Armitage

S. Desgreniers

S. Fafard

Gary W. Slater

LE DOYEN DE LA FACULTÉ DES ÉTUDES SUPÉRIEURES ET POSTDOCTORALES /
DEAN OF THE FACULTY OF GRADUATE AND POSTDOCTORAL STUDIES

DEVELOPMENT OF OFFSET LOCKING BASED
DISTRIBUTED SENSOR AND STUDY OF POLARIZATION
EFFECTS IN OPTICAL FIBERS

by

Ou Chen

A thesis submitted to the Faculty of Graduate and Postdoctoral Studies
University of Ottawa
in partial fulfillment of the requirements for the degree of

Master of Science

Department of Physics

University of Ottawa

April 2005



Library and
Archives Canada

Bibliothèque et
Archives Canada

Published Heritage
Branch

Direction du
Patrimoine de l'édition

395 Wellington Street
Ottawa ON K1A 0N4
Canada

395, rue Wellington
Ottawa ON K1A 0N4
Canada

Your file *Votre référence*
ISBN: 0-494-11236-0
Our file *Notre référence*
ISBN: 0-494-11236-0

NOTICE:

The author has granted a non-exclusive license allowing Library and Archives Canada to reproduce, publish, archive, preserve, conserve, communicate to the public by telecommunication or on the Internet, loan, distribute and sell theses worldwide, for commercial or non-commercial purposes, in microform, paper, electronic and/or any other formats.

The author retains copyright ownership and moral rights in this thesis. Neither the thesis nor substantial extracts from it may be printed or otherwise reproduced without the author's permission.

AVIS:

L'auteur a accordé une licence non exclusive permettant à la Bibliothèque et Archives Canada de reproduire, publier, archiver, sauvegarder, conserver, transmettre au public par télécommunication ou par l'Internet, prêter, distribuer et vendre des thèses partout dans le monde, à des fins commerciales ou autres, sur support microforme, papier, électronique et/ou autres formats.

L'auteur conserve la propriété du droit d'auteur et des droits moraux qui protègent cette thèse. Ni la thèse ni des extraits substantiels de celle-ci ne doivent être imprimés ou autrement reproduits sans son autorisation.

In compliance with the Canadian Privacy Act some supporting forms may have been removed from this thesis.

Conformément à la loi canadienne sur la protection de la vie privée, quelques formulaires secondaires ont été enlevés de cette thèse.

While these forms may be included in the document page count, their removal does not represent any loss of content from the thesis.

Bien que ces formulaires aient inclus dans la pagination, il n'y aura aucun contenu manquant.


Canada

Copyright © Ou Chen 2005

All Rights Reserved

ABSTRACT

This thesis is composed of two main sections.

The first section is the development of an optical fiber sensor. The application of optical fibers in the sensing field has boomed in recent years. Based on the Brillouin scattering effect in the optical fiber, various distributed temperature and strain sensors have been developed and commercialized. In our lab, we had used a continuous wave pump laser and a pulsed probe laser to obtain the counter-propagating Brillouin gain/loss spectrum. The two narrow linewidth diode-pumped Nd:YAG lasers used for the pump/probe beams are locked together to get the Brillouin spectrum along the optical fibers under test. To reduce the cost of the system, two distributed feedback lasers have replaced the diode-pumped Nd:YAG lasers. The offset locking technique and an optical delay line are applied in order to obtain stable and tunable Brillouin spectrum. In addition, this new sensor system has been simulated by a Matlab program that considers the distributed feedback lasers' broader linewidth compared with that of frequency stabilized Nd:YAG lasers.

The second section involves research on polarization effects in the optical fiber. In a high speed optical communication system with polarization mode dispersion and polarization dependent loss, the measurements usually involve finding four states of polarization to estimate the complex principle state of polarization vec-

tor. In this thesis it is proven that only three states of polarization are required to determine the principle state of polarization vector. In addition, polarization effects in fiber Bragg gratings are investigated in this work. To measure the polarization dependent loss of the fiber Bragg grating for the reflection wavelength, an optical circulator is used. A problem arises since the circulator's polarization dependent loss contributes to the measurement result; this effect is often ignored. In this thesis, a test set has been developed to eliminate this uncertainty effect through a three-step procedure using the Jones Matrix method.

CONTENTS

ABSTRACT	iv
LIST OF FIGURES	xi
ACKNOWLEDGMENTS	xii
I DEVELOPMENT OF OFFSET LOCKING BASED DISTRIBUTED SENSOR	xv
Chapter	
1 INTRODUCTION	1
2 BRILLOUIN SCATTERING	7
2.1 Nonlinear Effect and Brillouin Scattering	7
2.2 Brillouin Gain, Threshold and Coupled Intensity Equation	14
2.3 Applications of Brillouin Scattering	16
3 OFFSET LOCKING TWO DISTRIBUTED FEEDBACK LASERS	18
3.1 Semiconductor Laser and Its Frequency Fluctuation	19
3.2 Optical Delay Line	25
3.3 Photodetectors	26
3.4 Mixer	29
3.5 Feedback Circuit	35
4 DISTRIBUTED FIBER OPTIC SENSOR SYSTEM BASED ON TWO DISTRIBUTED FEEDBACK LASERS	41
4.1 System Configuration	41
4.2 Electro-Optic Modulation	43
4.3 Polarization Scrambler	45
4.4 Experimental Results	46
4.5 Simulation of Brillouin Scattering	51

5 CONCLUSION (PART I)	58
II STUDY OF POLARIZATION EFFECTS IN OPTICAL FIBERS	60
6 BACKGROUND	61
7 CHROMATIC DISPERSION AND POLARIZATION EFFECTS	65
7.1 The Physics of Polarization Effects	65
7.2 Mathematical Description of Polarization	67
8 POLARIZATION MODE DISPERSION AND POLARIZATION DEPENDENT LOSS MEASUREMENTS IN OPTICAL COMMUNICATION SYSTEMS	74
8.1 Equation of Motion	74
8.2 Experimental Results	78
9 MEASUREMENT OF POLARIZATION DEPENDENT LOSS IN FIBER BRAGG GRATINGS	81
9.1 The Physics of Fiber Bragg Gratings	81
9.2 PDL and PMD Measurement of FBG	82
10 SUMMARY (PART II)	89
Appendices	
A. ABBREVIATIONS	90
B. LIST OF SYMBOLS	92
C. THE SIMULATION CODE FOR BRILLOUIN SENSOR WITH BROAD SPECTRAL linewidth BY MATLAB 6.5	94
D. CURRICULUM VITAE	98
E. PAPERS, POSTERS AND PRESENTATIONS	98
REFERENCES	99

LIST OF FIGURES

1.1	B-OTDA setup. AOM: acoustic-optical modulator.	2
1.2	Injection locking setup. BPF: band-pass filter; Polari.: polarization controller.	3
1.3	Nd:YAG laser system setup. PD: photodetector; DC: directional coupler.	4
2.1	Energy level diagram. A molecule is excited to a higher energy state, then drops to a lower level and releases an acoustic phonon.	12
2.2	The graphical illustration of three wave vectors during the Stokes in- teraction process.	13
3.1	DFB laser structure.	20
3.2	Beat signal without feedback. The beat frequency is unstable without feedback circuit.	22
3.3	Laser frequency vs. input current [25].	23
3.4	Frequency offset locking system. The feedback circuit controls only one of the lasers (DFB 2). DFB 1, DFB 2: distributed feedback laser 1 and 2; Mixer: electrical signal mixer; Optical delay: motorized variable optical delay line; PD 1, PD 2: photodiode 1 and 2.	24
3.5	Double balanced four-diode ring mixer [27]. LO: local oscillation; IF: intermediate frequency; RF: radio frequency; D: diode.	31

3.6	Typical phase detector response [28].	32
3.7	Inverting amplifier: $V_{out} = -\frac{R_2}{R_1}V_{in}$ (p control).	35
3.8	Integration circuit: $V_{out}(t) = \frac{1}{RC} \int_0^t V_{in}(t)dt + V_{out}(t = 0)$	36
3.9	Block diagram for stablizing the laser frequency.	36
3.10	Mixer's output voltage vs. frequency.	38
3.11	The PI control feedback circuit. OP: operational amplifier.	39
3.12	Beat signal with feedback. Beat frequency is stable with the feedback circuit.	40
4.1	The 1550 nm sensor system setup. TC: temperature control; CC: cur- rent control; PG: pulse generator; DAC: digital to analog converter; DAS: data acquisition system; Pol. Control: polarization control.	42
4.2	Typical Lithium Niobate (LiNbO ₃) optical modulator [29].	45
4.3	Polarization control with a single wave plate with variable retardation and orientation. Shown here is an all-fiber approach with rotatable fiber squeezer [31].	46
4.4	Beat frequency stability. 20 kHz for standard deviation in 10 minutes.	47
4.5	The tuning of beat frequency. 925 MHz is achieved by tuning optical delay line.	48

4.6	Time domain signal for a 1.8 km long fiber (measured by OTDR). The vertical scale is mV (voltage) and the horizontal scales is 20 μ s (time) . Channel 1 is the pulse produced by EOM and it is sent into the fiber under test. Channel 2 is the CW beam received after travelling through the fiber under test.	49
4.7	Brillouin gain spectrum at the center of the 1.8 km fiber. The peak frequency is located at 10857 MHz.	50
4.8	Assume the pump (I_p) and Stokes (I_s) have many transitions along fiber length L. Consider the incident light as a linear combination of many incident beams at different frequencies.	53
4.9	The laser's line-width is 5 kHz. The pulse width of the probe beam is 50 ns. Total fiber length is 20 m. The FWHM of the Brillouin spectrum is 90 MHz.	56
4.10	The laser's line-width is 5 MHz. The pulse width of the probe beam is 50 ns. Total fiber length is 20 m. The FWHM of the Brillouin spectrum is 75 MHz.	57
6.1	An optical circulator's function. The light comes from A goes to B, cannot go into C. The light comes from B goes to C, cannot go into A.	63
6.2	Working principle of an optical circulator. The dot and vertical line represent horizontal and vertical polarized beams, respectively. . . .	63

7.1	Polarization states can be described using an elliptical display, a point on the Poincare sphere or a set of Stokes parameters [50].	69
7.2	The Agilent 8509 Lightwave Measurement System. The PDL information is derived from the Jones matrix of the test component [50]. A, B, U, V represent the Jones matrices for the elements indicated (the component under test, one test fiber and the two leading fibers, respectively).	72
8.1	The test setup for PMD measurements. The computer controls the two optical switches simultaneously. 3 lines between the two switches represent 3 states of polarization.	78
8.2	A comparison of DGD measurements using Jones Matrix eigen-value analysis and the new experimental method.	79
8.3	PDL test result for the PDL emulator. As we can see, it is not the same with the DAS test result in the following figure.. . . .	80
8.4	The differential attenuation slope (DAS) for the same emulator.	80
9.1	A FBG.	82
9.2	The configuration for measuring PMD and PDL of a FBG.	83
9.3	PDL measurements before using new approach. The PDL values are between 0.05 to 0.3 dB.	87
9.4	PDL measurements using new approach. The PDL values are between 0.1 to 0.24 dB.	88

ACKNOWLEDGMENTS

First of all, I would like to thank my supervisors Dr. Xiaoyi Bao and Dr. Liang Chen. I feel that it is hard to find appropriate words to entirely express my appreciation of them. They granted me the opportunity to continue my education, taught me wonderful courses, and guided me in complicated experiments, etc. They are hard-working professors with great knowledge, and are respected by me and many other people working in the field.

During the past years, I have really enjoyed the academic life in the fiber optic lab. I have to say I had very good colleagues in the lab. They were very warm-hearted and helpful, whenever you needed them. They are Yidun Wan, Lufan Zou, Shiquan Yang, Ping Lu, Guilin Wu, Graham Ferrier, Dan Falk, Saeed Hadjifaradji, Shahraam Afshar Vahid, Evgueni Ponomarev, David Waddy, Dongfeng Liu, Qingrong Yu, Xiaodong Zeng, Robert Walker, Fabien Ravet, Li Xie, Line Bouchard, Khalid Al-Qadi, Ziyi Zhang, etc.

I also would like to thank John Bernard from the NRC for help with experiments and the people from the Department of Physics at the University of Ottawa for their general help.

Special thanks go to Paul Beckwith for reviewing this thesis!

Many thanks go to ISIS Canada and NSERC for their financial support.

Finally, I thank all my family, who were always there encouraging me to do

better work!

With all your help, this thesis comes true!

STATEMENT OF ORIGINALITY

I certify that this thesis, and the research to which it refers, are the product of my own work, and that any ideas or quotations from the work of other people, published or otherwise, are fully acknowledged in accordance with the standard referencing practices of the discipline. I acknowledge the helpful guidance and support of my supervisors, Professor Xiaoyi Bao and Professor Liang Chen. I am indebted to Liang Chen for the derivation of the polarization mode dispersion measurement in a polarization dependent loss and polarization mode dispersion combined system [Chapter 8], Ping Lu for the configuration of polarization dependent loss measurement for fiber Bragg gratings [Chapter 9], and Guilin Wu and Dan Falk for the discussion on the offset locking technique [Chapter 3]. The included manuscripts presented in conferences or journal publications are listed in the section of "Papers, posters and presentations. The work has not been presented previously for any degree, nor is it at present under consideration by any other degree awarding body.

Ou Chen

Ottawa 2005

Part I

**DEVELOPMENT OF OFFSET
LOCKING BASED
DISTRIBUTED SENSOR**

CHAPTER 1

INTRODUCTION

A sensor is a device that responds to a physical stimulus (such as heat, light, sound, pressure, magnetic or electric field, or a particular motion) and transmits a resulting impulse (as for measurement or operating a control) [Source: Merriam-Webster Medical Dictionary, ©2002 Merriam-Webster, Inc.]. For example, a bridge could be monitored with a sensor in order to determine its structural strain variation with time. By doing so, civil engineers could reinforce the bridge before it collapses so as to protect people's lives and property.

The optical fiber has an interesting and useful nonlinear optical effect: Brillouin scattering. This effect can be utilized to convert ordinary optical fibers into sensors. Scientists developed the Brillouin scattering based optical time domain analysis method to make optical fiber based temperature and strain sensors [1]. By sending pulsed light (probe) and CW light (pump) into opposite ends of the fiber, and measuring the Brillouin spectrum at each position along the fiber, one can find the temperature or strain distribution along the fiber-attached structure. The spatial resolution is determined by the width of the pulse launched into the optical fiber.

There are three major groups in the world working on Brillouin scattering based optical fiber sensors. The group at NTT uses a counter-propagating light configuration to obtain the stimulated Brillouin gain spectrum [1]. Its block dia-

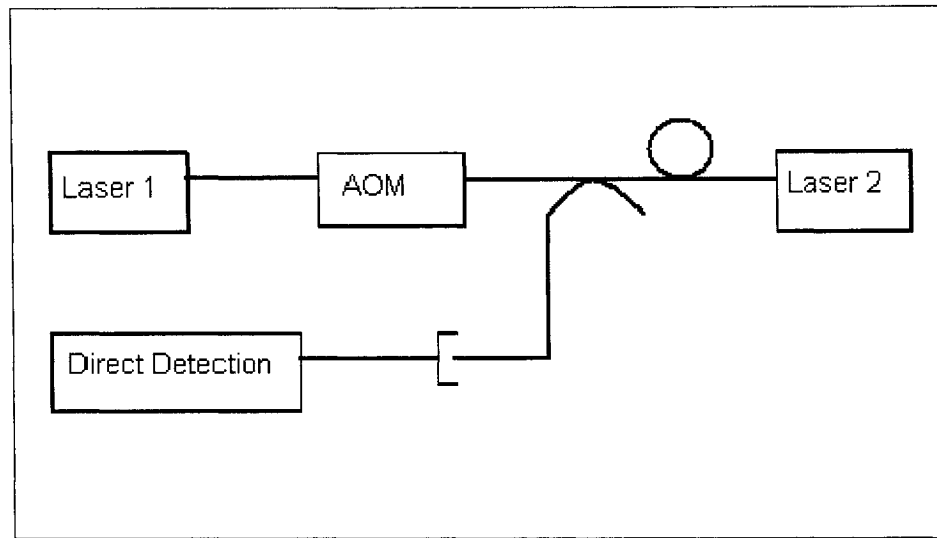


Figure 1.1: B-OTDA setup. AOM: acoustic-optical modulator.

gram is shown in Figure 1.1 [9]. The AOM generates pulses from CW laser 1.

The research group at the Swiss Federal Institute of Technology once used an EOM and microwave generator to generate both pulsed and CW probe lightwaves from a single laser source to realize the distributed Brillouin gain spectrum measurement, and recently they also propose an injection-locking technique to stabilize the relative frequency in the two lasers system [3]. The lower sideband of the distributed feedback laser is amplified in B-OTDA, and the upper sideband is depleted. Its block diagram is shown in Figure 1.2, laser 1 is driven by an RF (radio frequency) signal to generate the pulses.

The research group at the University of Ottawa, headed by Dr. Xiaoyi Bao and Dr. Liang Chen, uses a similar setup (shown in Figure 1.3) to implement B-OTDA [2]. The major difference between this setup and the previous one is that a combination of CW and pulse is used as the probe signal instead of pulse

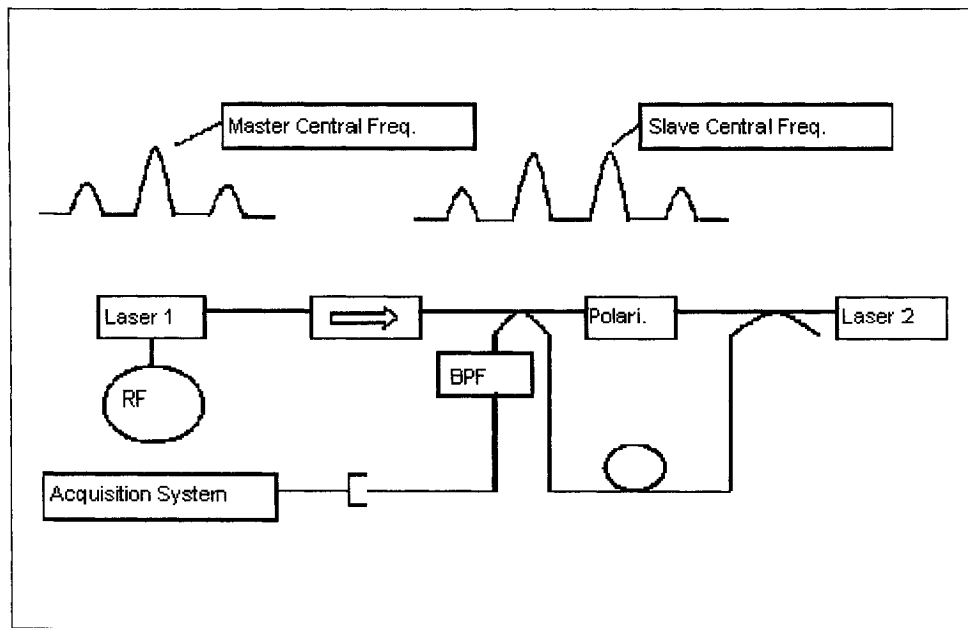


Figure 1.2: Injection locking setup. BPF: band-pass filter; Polari.: polarization controller.

alone. This improvement brings coherent interactions between the pump and probe beams. The initial experimental results, namely a temperature resolution of 1°C and a spatial resolution of 10 m for a 22 km long fiber were achieved [4] in the early 1990s when Dr. Bao worked at the University of Kent. Later on, the experiments at the University of New Brunswick showed 10 cm spatial resolution and 40 - 50 micro-strain accuracy [2]. The recent developments at University of Ottawa will be introduced in the next chapter.

As shown in Figure 1.3, both lasers launch a CW pump beam, and light from one laser is modulated by an electro-optic modulator to produce a combined pulsed and CW beam (Stokes probe). The two beams are launched into the sensing fiber at the opposite ends of the fiber. Due to the Brillouin amplification, the Stokes

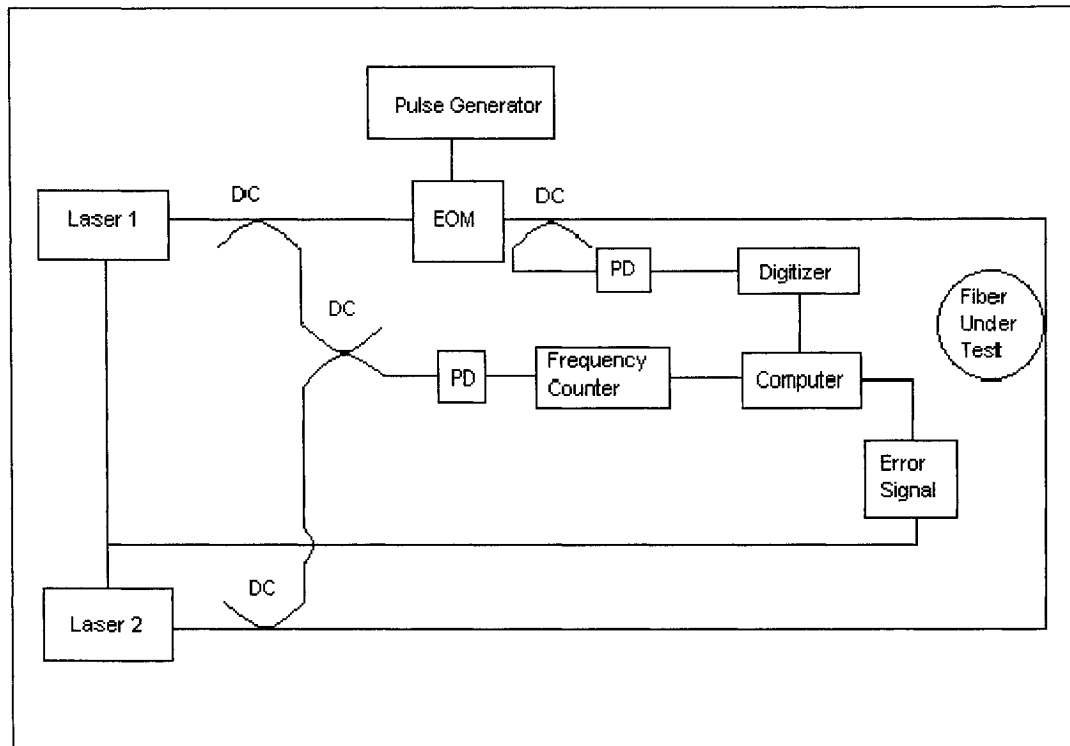


Figure 1.3: Nd:YAG laser system setup. PD: photodetector; DC: directional coupler.

wave is continually amplified as it travels through the sensing fiber at the expense of the pump beam; the depletion in CW pump power is measured over a range of different frequency to create the Brillouin loss spectrum. The use of a pulsed probe beam allows the system to take separate measurements of the Brillouin spectrum in different regions along the fiber. Therefore, a 3-D data set in position (corresponding to time), frequency and power loss is formed. Finally, we obtain time-domain Brillouin scattering signals and Brillouin spectrums along the optical fiber at a certain spatial resolution. As the Brillouin shift depends on the effective refractive index of the fiber, it changes whenever the refractive index of the silica in the fiber changes in response to local environmental variations (such as temperature and strain etc.). By monitoring the Brillouin frequency shift along the fiber length, we can successfully map out the distribution of temperature and strain.

The lasers normally used for this technique are frequency stabilized Nd:YAG lasers operating at a 1319 nm wavelength (made by Lightwave Electronics, with model numbers 125-1319-200 and 125-1319-150). The linewidth of this laser is 5 kHz measured over one millisecond, and thus can be ignored when compared to a Brillouin gain bandwidth of about 35 MHz for standard SMF-28 fiber [1]. In this system, a beat frequency stability of 1.25 MHz can achieve 1°C temperature accuracy [4] or 24 micro-strain accuracy [1] [Micro-strain: Strain expressed as parts of million (ppm)]. However, these Nd:YAG lasers are very expensive which limits its practical application. In this work, we try to replace them with commonly available DFB semiconductor lasers and use the offset locking technique to build

a new sensor system. The offset locking technique refers to the frequency offset locking, which was proposed as a reliable electrical negative feedback technique for producing a radio frequency signal from a two-semiconductor-laser system [5]. The difference between the beat frequency (of two DFB lasers) and the desired frequency can be used as an error which would be fed back into one of the laser current sources in order to change the beat frequency to a stable desired frequency by forcing the error to zero. In our new sensing system, two NTT Electronics Corporation produced DFB lasers and a General Photonics Corporation produced optical delay line are used. The frequency stabilized signal can be tuned in a large frequency range (about 1 GHz) by applying the optical delay line. This system has two main benefits over the previous system. One is to reduce the cost of the lasers themselves by moving the operating wavelength from 1310 nm to 1550 nm, second is to reduce fiber loss at 1550 nm which can increase the sensing range.

In the following three chapters of Part I, this thesis will introduce the Brillouin scattering principle, the offset locking technique and the sensor system setup and simulation. Finally in Chapter 5, there is a brief conclusion for this sensor section.

CHAPTER 2

BRILLOUIN SCATTERING

2.1 Nonlinear Effect and Brillouin Scattering

When light is launched into silica, the interaction occurring between the radiation and material is a combination of linear and nonlinear processes. The linear responses are measured in terms of the polarization induced in the material by the input electric field. The linear processes include superposition, reflection, refraction, birefringence and absorption, which are covered by classical optics. The nonlinear processes include parametric and inelastic processes, which happen when the input electric field is intense and coherent. Brillouin scattering is one of the inelastic processes. If the material is an optical fiber, the nonlinear effect will be large due to the small spot size and very low loss of the fiber (high intensity). If the material is bulk silica, the nonlinear effect will be small since the intensity is lower (the light is not guided).

In the linear case, the electric dipole induced polarization under the electric field can be expressed as [[6], page 12]:

$$\begin{aligned} P_x &= \varepsilon_0(\chi_{11}E_x + \chi_{12}E_y + \chi_{13}E_z) \\ P_y &= \varepsilon_0(\chi_{21}E_x + \chi_{22}E_y + \chi_{23}E_z) \\ P_z &= \varepsilon_0(\chi_{31}E_x + \chi_{32}E_y + \chi_{33}E_z) \end{aligned} \tag{2.1}$$

where ε_0 is the electric permittivity of vacuum and χ is the linear susceptibility. One can choose a coordinate system so that the off-diagonal elements vanish, thus one has:

$$P_x = \varepsilon_0 \chi_{11} E_x \quad (2.2)$$

$$P_y = \varepsilon_0 \chi_{22} E_y$$

$$P_z = \varepsilon_0 \chi_{33} E_z$$

In general case, the electric dipole induced polarization is expressed as a power series of the electromagnetic field. It is given by [[8], page 17]:

$$P = \varepsilon_0 (\chi^{(1)} E + \chi^{(2)} E^2 + \chi^{(3)} E^3) \quad (2.3)$$

where:

$\chi^{(1)}$ is the linear susceptibility, which is a complex number due to the definition $P = \varepsilon_0 \chi^{(1)} E$ in linear optics. It is related to the refractive index n ($n = 1 + \frac{1}{2} \text{Re} \chi^{(1)}$) [7] and the attenuation coefficient α ($\alpha = \frac{\omega}{nc} \text{Im} \chi^{(1)}$) [[8], page 33] by using the definitions $\varepsilon = 1 + \chi$ and $\varepsilon = (n + i\alpha c/2\omega)$. ω is the optical angular frequency.

$\chi^{(2)}$ is the second order susceptibility and vanishes in silica fiber because of symmetry (centrosymmetric);

$\chi^{(3)}$ is the third order susceptibility and leads to four-wave mixing, Raman scattering and Brillouin scattering among other effects.

The refractive index change induced in the optical fiber by the input optical field intensity can be written as [[8], page 18]:

$$\tilde{n}(\omega, |\vec{E}|^2) = n(\omega) + n_2 |\vec{E}|^2 \quad (2.4)$$

where $|\vec{E}|^2$ is the optical intensity, $n(\omega)$ represents the index with no applied optical field, and n_2 is the nonlinear index coefficient related to $\chi^{(3)}$.

Intensity related nonlinear refraction causes two elastic effects: Self-phase modulation (SPM) in ultrashort pulses or solitons and Cross-phase modulation (XPM) with two optical input fields. These are elastic effects, so called parametric nonlinear processes, which means that no energy exchanges between the light and the medium.

There are also inelastic scattering effects which involve molecular vibration or density vibration of the material. The process can be described in this simple way: A photon of the incident field (pump) is annihilated to create a lower frequency photon (Stokes) and a phonon in the lattice of the material to conserve total energy and momentum. In this process, the optical field transfers part of its energy to the nonlinear medium. The two possible processes are Raman scattering (optical phonon created) and Brillouin scattering (acoustic phonon created). Raman scattering involves creation of optical phonons, which happens in both directions of the fiber. The Raman gain (in optical fibers) has a 30 THz spectral range and a spectral peak located near 13 THz. The gain coefficient is typically 7×10^{-14} m/W. The stimulated Raman scattering threshold is defined as the input pump power

at which the Stokes power becomes equal to the pump power at the fiber output. Then the pump power required to reach the Raman threshold is about 600 mW for a fiber with an effective length of 20 km at 1550 nm wavelength [[8], page 303]; where effective length is defined as [[8], page 301]:

$$L_{eff} = \frac{1 - \exp(-\alpha L)}{\alpha} \quad (2.5)$$

where α is the fiber loss, $\alpha = \frac{\alpha_{dB}}{4.343} = \frac{0.2(\text{dB/km})}{4.343} = 0.0461 \times 10^{-3} \text{m}^{-1}$.

The Brillouin scattering process under steady-state conditions (applicable for a CW or quasi-CW pump) can be expressed by the coupled equations [[8], page 360]:

$$\begin{aligned} \frac{dI_p}{dz} &= -g_B I_p I_S - \alpha I_p \\ \frac{dI_S}{dz} &= -g_B I_p I_S + \alpha I_S \end{aligned} \quad (2.6)$$

where I_S is the Stokes intensity (W/m^2), I_p is the pump intensity (W/m^2), Brillouin gain coefficient g_B is typically $6 \times 10^{-11} \text{ m}/\text{W}$.

Brillouin Scattering (BS) involves creation of acoustic phonons, which happens mainly in the backward direction of the fiber. It has a less than 100 MHz spectral range and the Stokes shift is about 11 GHz in optical fiber near 1550 nm. The stimulated Brillouin scattering threshold is defined as the input pump power at which the Stokes power becomes equal to the pump power at the fiber output. The pump power required to reach the Brillouin threshold is about 1 mW at 1550 nm wavelength for a 20 km effective length fiber [[8], page 361]. This effect can be used

to design Brillouin scattering based Optical Time Domain Analysis (B-OTDA).

In a multichannel optical telecommunication system, the stimulated Brillouin scattering limits the channel powers, because part of the channel power can be transferred to a backward-propagating Stokes wave generated from noise when the threshold condition is satisfied. However, for non telecommunication applications, this phenomenon is useful to make fiber lasers, amplifiers and sensors.

Classically, Brillouin scattering is a nonlinear interaction between the pump and Stokes optical fields through an acoustic wave. The pump field generates an acoustic wave through the process of electrostriction. [Electrostriction: Property of all electrical nonconductors, or dielectrics, that manifests itself as a relatively slight reduction of size, or mechanical deformation, under the application of an electric field. Reversal of the electric field does not reverse the direction of the deformation. [9]] The acoustic deformation (wave) in turn modifies (modulates) the refractive index of the medium. This pump-induced index grating scatters the pump light through Bragg diffraction. Scattered light is downshifted in frequency because of the Doppler shift associated with scattering from a grating moving away at the acoustic velocity v_A .

Quantum-mechanically, Brillouin scattering is the annihilation of a pump photon creating a Stokes photon and an acoustic phonon simultaneously [[8], page 356].

Due to the conservation of total energy and momentum, as shown in Figure 2.1, one has:

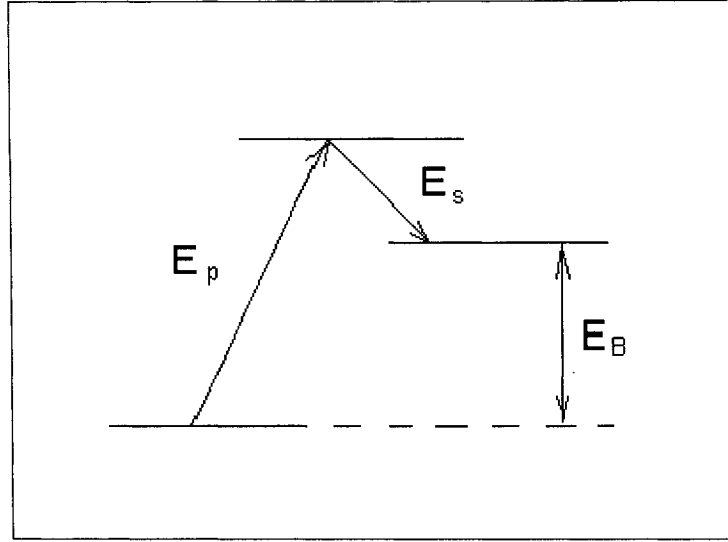


Figure 2.1: Energy level diagram. A molecule is excited to a higher energy state, then drops to a lower level and releases an acoustic phonon.

$$E_p = E_s + E_B \quad (2.7)$$

$$\hbar\omega_p = \hbar\omega_s + \hbar\omega_B$$

which results in

$$\omega_B = \omega_p - \omega_s \quad (2.8)$$

where subscripts p and s represent the pump and Stokes, B means Brillouin, ω is the optical angular frequency, and ω_B is the Brillouin angular frequency;

In Figure 2.2, one has:

$$\vec{k}_A = \vec{k}_p - \vec{k}_s \quad (2.9)$$

where A means acoustic, k is the wave vector, θ is the angle between the pump

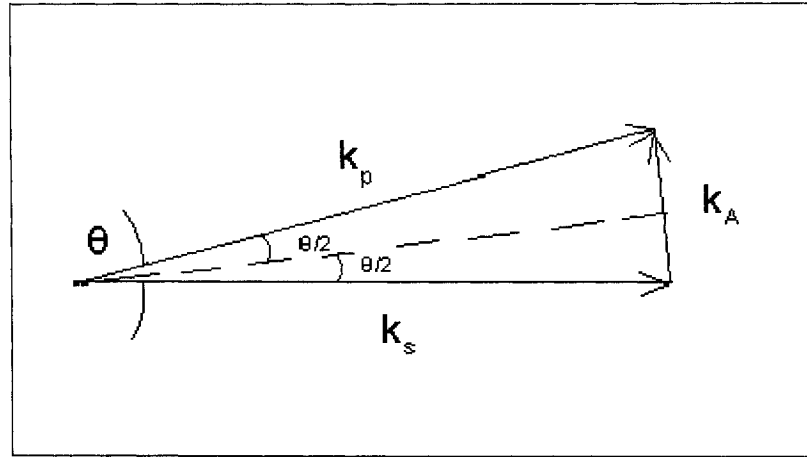


Figure 2.2: The graphical illustration of three wave vectors during the Stokes interaction process.

and Stokes fields.

and

$$|\vec{k}_A| = 2 |\vec{k}_p| \sin(\theta/2) \quad (2.10)$$

By the dispersion relation,

$$\omega_B = v_A |\vec{k}_A| \approx 2v_A |\vec{k}_p| \sin(\theta/2) \quad (2.11)$$

We assume $|\vec{k}_p| \approx |\vec{k}_s|$ and we know $|\vec{k}_p| = 2\pi n/\lambda_p$. In single mode fibers, for backward Brillouin scattering ($\theta = 180^\circ$), the Brillouin frequency shift is:

$$\nu_B = \omega_B/2\pi = 2nv_A/\lambda_p \quad (2.12)$$

For a Corning SMF-28 optical fiber, using $v_A = 5.750$ km/s [10] and $n = 1.4675$ [11] then we have Brillouin frequency $\nu_B \approx 12795$ MHz for $\lambda_p = 1319$ nm (Nd:YAG

lasers in our lab) or $\nu_B \approx 10860$ MHz for $\lambda_p = 1554$ nm (DFB lasers in our lab).

2.2 Brillouin Gain, Threshold and Coupled Intensity Equation

The Brillouin gain spectrum $g_B(\omega)$ characterizes the growth of the Stokes wave. At the Brillouin frequency ω_B , the gain g_B has its maximum. The phonon lifetime T_B is related to the acoustic damping rate Γ_B as follows: $T_B = \Gamma_B^{-1} \sim 10$ ns. The spectral width (about tens of MHz [[8], page 357]) of the gain spectrum is related to the damping time of acoustic waves. If acoustic waves are assumed to decay as $\exp(-\Gamma_B t)$, the Brillouin gain has a Lorentzian spectrum of the form [[8], page 357]:

$$g_B(\omega) = g_p \frac{(\Gamma_B/2)^2}{(\omega - \omega_B)^2 + (\Gamma_B/2)^2} \quad (2.13)$$

The peak value of the Brillouin gain coefficient occurring at $\omega = \omega_B$ is found to be:

$$g_p \equiv g_B(\omega_B) = \frac{2\pi^2 n^7 p_{12}^2}{c \lambda_p^2 \rho_0 v_A \Gamma_B} \quad (2.14)$$

where p_{12} is the longitudinal elasto-optic coefficient and ρ_0 is the material density. The full-width-half-maximum (FWHM) of the Brillouin gain spectrum is $\Delta\nu_B = \Gamma_B/2\pi$. Typically, $g_p \approx 5 \times 10^{-11}$ m/W. It is 3 orders of magnitude larger than the Raman gain coefficient.

The inhomogeneity in the fiber core cross section along the fiber length leads to the broadening of the Brillouin gain bandwidth, which can be as large as 100

MHz for the 1550 nm spectral region.

The Brillouin spectrum refers to the Brillouin loss spectral profile in the setup of B-OTDR. It is determined by not only the Brillouin gain spectrum, but also the frequency spectrum of input pulse.

Above contents are for steady-state conditions and are valid for CW or quasi-CW pump only, i.e. pulse width $T_0 \gg$ phonon lifetime T_B , which means that the spectral width (for a CW pump) $\Delta\nu_p \ll \Delta\nu_B$. When $T_0 < T_B$, or $\Delta\nu_p > \Delta\nu_B$, the Brillouin gain is reduced significantly that we are no longer at steady state. For instance when T_0 is less than 1 ns, the Brillouin gain is much reduced to a level even below that of the Raman gain [[8], page 359].

Let us assume the frequency $\omega_p \approx \omega_s$ and fiber loss $\alpha_p \approx \alpha_s \equiv \alpha$. The pump and Stokes beams have the same linear polarization direction. Then we have steady-state coupled equations: Equ.2.6:

If we neglect pump depletion ($\frac{dI_p}{dz} = 0$),

$$I_p(z) = I_p(0)e^{-\alpha z} \quad (2.15)$$

and the Stokes intensity [[8], page 360] is:

$$I_s(0) = I_s(L) \exp(g_B P_0 L_{eff} / A_{eff} - \alpha L) \quad (2.16)$$

where $P_0 = I_p(0)A_{eff}$ is the input pump power, A_{eff} is the effective core area, and L_{eff} is the effective length in Equation 2.5.

The Brillouin threshold occurs when [12]:

$$g_B P_{th} L_{eff} / A_{eff} \approx 21 \quad (2.17)$$

The threshold pump power P_{th} is about 1 mW with the conditions: $\lambda = 1.55 \mu\text{m}$, $A_{eff} = 50 \mu\text{m}^2$, $L_{eff} = 20 \text{ km}$, and $g_B = 5 \times 10^{-11} \text{ m/W}$.

If the state of polarization is scrambled, then the Brillouin scattering threshold P_{th} is increased by 50% and Brillouin gain g_B is reduced in that case by a factor of 1.5 [13].

2.3 Applications of Brillouin Scattering

Since the Brillouin frequency shift depends on the effective refractive index of the fiber mode, when the local environment changes causing strain or temperature change then the index will change, and thus we can use Brillouin scattering as a distributed sensor over a long distance, with the pulse signal timing used to extract the position information. The experiments are done as follows: one tunable CW probe and one pulsed pump laser are launched into the two opposite ends of a fiber. The CW signal is amplified ($\nu_{pump} < \nu_{probe}$) or depleted ($\nu_{pump} > \nu_{probe}$) when the magnitude of the difference of pump and probe frequencies matches the Brillouin shift.

As a material property (the refractive index of silica varies with both temperature and strain), the Brillouin frequency has a direct linear relationship with strain and temperature given by [7]

$$\nu_B = \nu_{B0} + C_T(T - T_0) + C_\epsilon(\epsilon - \epsilon_0) \quad (2.18)$$

where T_0 and ϵ_0 are the temperature and strain corresponding to a reference Brillouin frequency ν_{B0} . The temperature and strain coefficients, C_T and C_ϵ , are material properties representing the temperature-frequency and strain-frequency coefficients. $C_T \approx 1.22$ MHz/ $^\circ\text{C}$ [14]; $C_\epsilon \approx 0.058$ MHz/micro-strain [2] for SMF-28 fiber with a 1.32 μm Nd:YAG laser source.

The recently obtained spatial resolution is 15 cm along a single photonic crystal fiber with Nd:YAG lasers working at 1319 nm wavelength [15], strain resolution is 15 micro-strain in the same condition [15] and temperature resolution is 1 $^\circ\text{C}$ with a spatial resolution of 5 meter for a 32-km single mode fiber[16]. The Brillouin scattering technique has been applied to detect cracks in carbon fiber reinforced plastic (CFRP) [17], to measure the strain of a loading test on a bridge [18], to set a fire alarm [19] and to test strain in a pipeline [20].

The laser performance is very critical to the sensor system. In the next chapter, I will describe how to achieve offset-locking of two DFB lasers.

CHAPTER 3

OFFSET LOCKING TWO DISTRIBUTED FEEDBACK LASERS

A highly sensitive to temperature and strain, distributed, and cost effective sensor system would be extremely useful for structural monitoring in civil engineering applications. In our lab, we are trying a distributed Brillouin scattering fiber optic sensing system working at 1550 nm wavelength using distributed feedback lasers. DFB lasers are compact in size and are low cost (less than \$1000 each), but the frequency stability is in the range of 1 - 10 MHz. To stabilize the beat frequency of two DFB lasers at the Brillouin frequency, we use the frequency offset locking technique with an optical delay line and an electrical feedback circuit [5]. We have thus converted the 1310 nm sensor system to the 1550 nm wavelength, which is the most commonly used wavelength region in modern fiber optic telecommunication systems (low loss).

The difference between the beat frequency (of two DFB lasers) and the desired frequency can be used as an error which would be fed back into one of the laser current sources in order to change the beat frequency to a stable desired frequency by forcing the error to zero, therefore the frequency difference between the two sources is locked to this desired frequency with high stability. This is called "Offset locking technique". In some cases, one source frequency is fixed, for instance in the case of a local oscillator. In another case, neither of the two source frequencies fixed, and one applies an optical delay line to obtain a frequency difference

between the two sources [21]. There are phase locked loop circuits [22] and optical injection locking methods [23] to stabilize the frequency. In this work, we use a PI (proportional integrating) control feedback circuit to lock the phase difference of the beat frequency and the desired frequency.

3.1 Semiconductor Laser and Its Frequency Fluctuation

The semiconductor laser emerged in 1970s. It is fabricated based on stimulated emission of photons through optical transition of electrons in a semiconductor material, i.e. GaAs. For achieving the population inversion, usually, the excitation by current injection is used to produce a large number of electron-hole pairs. Then a pair of cleaved facets were also made to implement coherent optical wave amplification. There are lateral modes and longitudinal modes in a semiconductor laser. The lateral mode, which has a distribution in the cross section normal to optical axis, is defined by waveguide structure. The longitudinal mode corresponds to m , in which $2L = m\lambda$, where λ is wavelength and L is length between facets. Naturally, in a continuous oscillation, variations in the injection current and ambient temperature give rise to a change in the longitudinal mode. To maintain a single-mode oscillation in a dynamic operation, an optical resonator is needed. This results in a birth of distributed feedback (DFB) lasers. The DFB laser [Figure 3.1] is a semiconductor laser developed in the 1980s. The device has a grating written on the semiconductor substrate, grown in multi-layers by the epitaxial method. The Bragg reflection grating in the active region suppresses multiple longitudinal modes and enhances a single longitudinal mode so that the lasing wavelength can

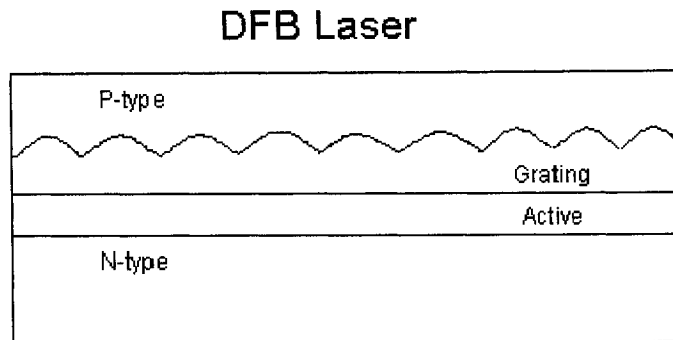


Figure 3.1: DFB laser structure.

be selected (and have single mode operation). Lasers with different wavelengths can be manufactured by changing the period of the grating.

The semiconductor laser has a frequency fluctuation coming from the index fluctuation associated with the carrier fluctuation and the spontaneous emission to the oscillation mode. As we know, the population inversion in the semiconductor lasers is realized through the injection of minority carriers with a high energy in the vicinity of a P - N junction by supplying an external forward current. The current fluctuation will cause the carrier density fluctuation so that the index fluctuation induced by the carrier density fluctuation dominates the frequency noise. And the frequency noise due to spontaneous emission coupling to the oscillation mode always remains. The noise spectrum can be written by [[24], page 212]:

$$S_\omega(\omega_m) \approx \frac{C_s N}{2\tau_s S} [\alpha_c^2 |H(\omega_m)|^2 + 1] \quad (3.1)$$

where S_ω is the noise power spectrum, ω_m is the modulation frequency, C_s is the ratio of the number of photons belonging to the same mode as the laser oscillation mode to the total number of spontaneous emission photons, N is the density of the minority carriers (electrons in the conduction band), τ_s is spontaneous emission time, S is the photon density over the volume of the resonator, α_c is carrier-induced refractive index change, it is also called a linewidth enhancement factor, $H(\omega_m)$ is the normalized complex transfer function which describes the transfer of modulation from the current to optical output. Obviously, C_s and α_c should be reduced and the laser should be operated with a high bias level (high output power) in order to reduce the frequency noise. The semiconductor laser's spectrum has a finite linewidth which is closely related to the frequency noise from the fluctuation in the refractive index caused by the fluctuation in the high-density carriers. With external cavity DFB lasers, one can get a spectral width of a few kHz. Thus, the fluctuation in the high-density carriers can be compensated.

The semiconductor laser's linewidth $\delta\omega_{semi}$ can be expressed by [[24], page 224]:

$$\delta\omega_{semi} = \frac{C_s N}{2\tau_s S} [\alpha_c^2 + 1] \quad (3.2)$$

Since α_c is usually larger than unity, the index fluctuation dominates the linewidth. The linewidth is inversely proportional to the photon density over the

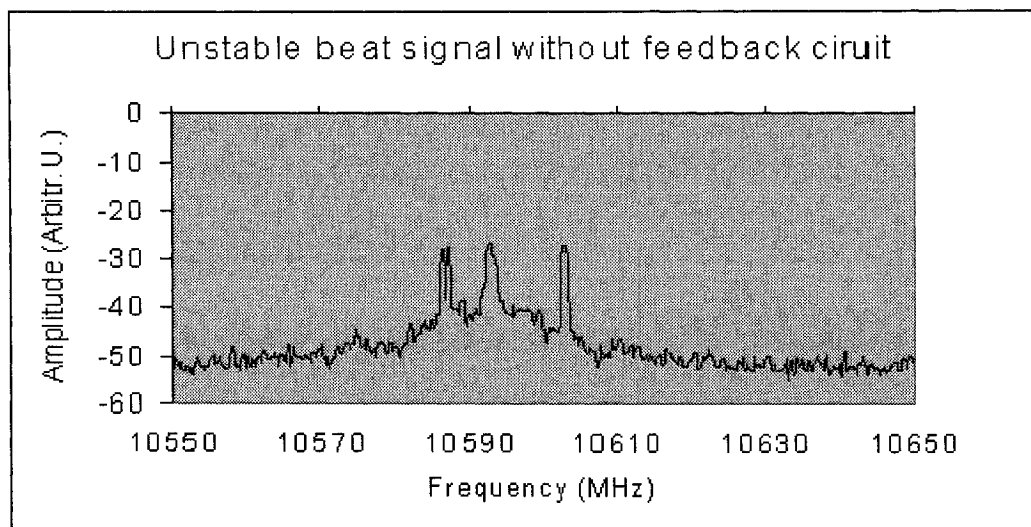


Figure 3.2: Beat signal without feedback. The beat frequency is unstable without feedback circuit.

volume of the resonator. Most common semiconductor lasers have a linewidth of several MHz to tens of MHz.

In the following system, we use two 20 mW DFB lasers (at 1554.35 nm and 1554.37 nm wavelengths). The spectral width is about 5 MHz, and the frequency stability over a few seconds is shown in Figure 3.2. When the two lasers are free running, the beat signal produced is very poor in stability. Thus, in the following section, I describe in detail how to stabilize this beat note.

Although a temperature controller is used to coarsely control each of the laser's output frequencies, only current control is used to adjust laser frequency, because the frequency response of the DFB laser for current change is much faster than

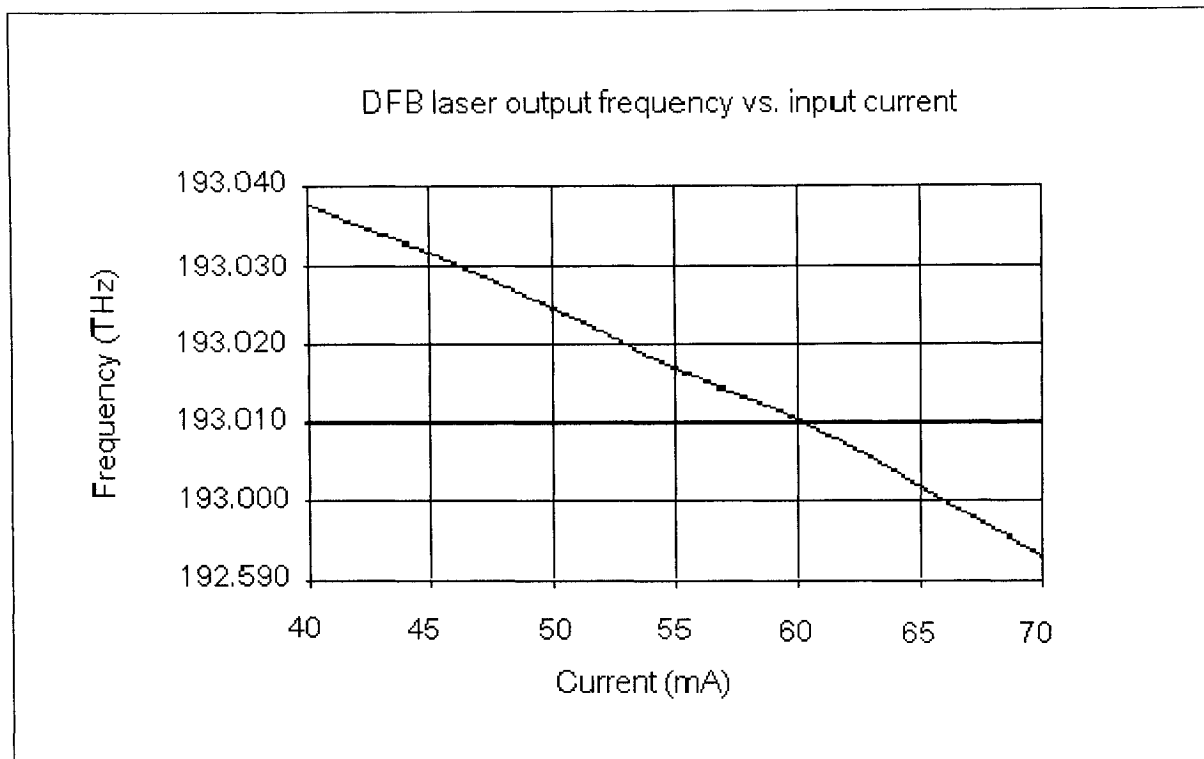


Figure 3.3: Laser frequency vs. input current [25].

that for temperature change. (Verified experimentally by conducting simple tests). The two lasers were kept at same temperature unchanged, so that we could ignore any temperature effect. The Laser Diode (LD)'s frequency was tuned by changing the current only, following the frequency vs. current curve shown in Figure 3.3. And the current is controlled through an external modulation input signal to the ILX Lightwave's LDX-3620 current source.

The configuration of the frequency offset locking system is shown in Figure 3.4. When two lasers are used for the Brillouin scattering sensor system, a very stable frequency difference between the two lasers is required. This is referred to as the frequency set-point ΔW (the desired beat note frequency to match the Brillouin

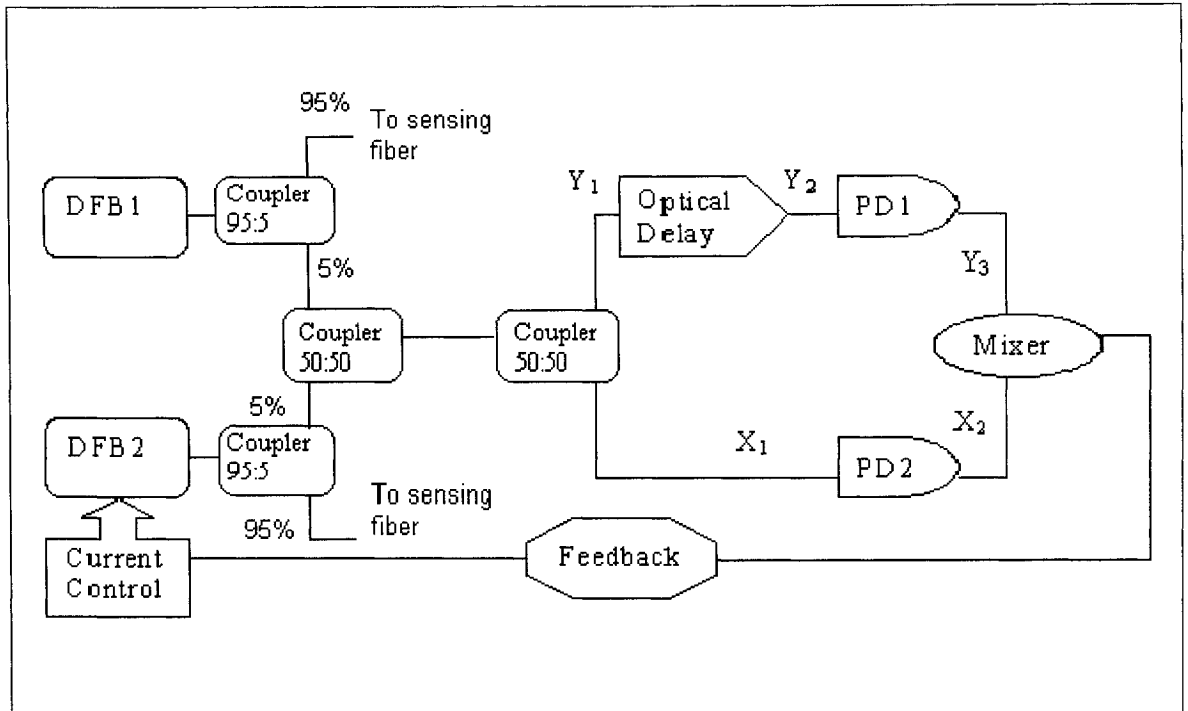


Figure 3.4: Frequency offset locking system. The feedback circuit controls only one of the lasers (DFB 2). DFB 1, DFB 2: distributed feedback laser 1 and 2; Mixer: electrical signal mixer; Optical delay: motorized variable optical delay line; PD 1, PD 2: photodiode 1 and 2.

frequency, for instance $\simeq 10860$ MHz for the 1554 nm DFB lasers). The feedback loop adjusts one laser to follow the other laser in frequency ω by continuously adjusting the change in frequency $\Delta\omega$ (via current changes) so that the error $\delta\omega$ is at or near zero.

$$\delta\omega = \Delta\omega - \Delta W \quad (3.3)$$

Assume that the laser outputs are $E'_{01} \sin(\omega_1 t - \phi'_1)$ and $E'_{02} \sin(\omega_2 t - \phi'_2)$,

where E'_{01} and E'_{02} are the electrical amplitudes of laser 1 and 2; ϕ'_1 and ϕ'_2 are the electrical phases of laser 1 and 2; while ω_1 and ω_2 are the optical frequencies of laser 1 and 2, respectively. A coupler at the laser outputs sends 95% of the laser signal to the sensor fiber and 5% of the signal into the feedback loop. The feedback loop signals are coupled together into one fiber through the use of a 50:50 coupler. For simplicity, due to the very short fiber length between couplers, we can neglect the fiber loss. The output from the second 50:50 coupler is comprised of two equal parts, Y_1 and X_1 :

$$Y_1 = E_{01} \sin(\omega_1 t - \phi_1) + E_{02} \sin(\omega_2 t - \phi_2) \quad (3.4)$$

$$X_1 = E_{01} \sin(\omega_1 t - \phi_1 + \phi_a + \frac{\pi}{2}) + E_{02} \sin(\omega_2 t - \phi_2 + \phi_b + \frac{\pi}{2})$$

where E_{01} and E_{02} are the amplitudes after passing the couplers; ϕ_1 and ϕ_2 are the optical phases after going through the couplers; and ϕ_a and ϕ_b are the optical phase differences induced by the path length difference of Y_1 and X_1 for ω_1 and ω_2 , respectively. The $\frac{\pi}{2}$ phase shift arises from the second 50:50 coupler.

3.2 Optical Delay Line

Since we can only control $\Delta\omega$ implicitly through the feedback control loop, the optical delay Δt is used to scale the change of phase $\Delta\omega\Delta t$. In the experiments, a motorized variable optical delay line is used. This device provides precision optical path length adjustment. Driven by a DC motor with an integrated encoder, the motorized delay line has a micrometer delay resolution. The device has an

optical delay range of 600 ps which is corresponding to a 180 mm free space path length distance. This is the longest optical delay line available in the market. By conducting frequency sweeping around 10860 MHz, a 925 MHz beat frequency tuning range was achieved. Through the relationship of $(\omega_0 + \omega')t_0 = \omega_0(t_0 + t')$, where ω_0 is the reference frequency, t_0 is the reference time delay, ω' is the frequency range and t' is the optical delay change, we can draw the conclusion that the longer the optical delay is, the bigger the frequency range is. This optical delay line has 10 speed settings for changing delay time, from 0.01 ps/sec to 250 ps/sec. The faster the delay time changes, the less time the test of Brillouin spectrum sweeping needs. In our setup, 1 ps/sec speed is most often chosen by evaluate the experimental results.

When signal Y_1 passes through the optical delay line it experiences a delay of Δt , then we have:

$$Y_2 = E_{01} \sin[\omega_1(t - \Delta t) - \phi_1] + E_{02} \sin[\omega_2(t - \Delta t) - \phi_2] \quad (3.5)$$

3.3 Photodetectors

The photodetector is composed of semiconductor material with a p-n junction, and converts the optical signal to an electrical signal through the photoelectric effect. An electron-hole pair will be generated in the material when an incident photon with energy $h\nu$ greater than the band-gap energy is absorbed by the material. These pairs form a photocurrent I_p after applying a reverse-bias electric field. The photocurrent is proportional to the incident optical power P_{in} [[26], page 134]:

$$I_p = R * P_{in} \quad (3.6)$$

where R is responsivity of the photodetector. The responsivity is related to the incident light wavelength and the quantum efficiency, for our case, it is assumed to be constant. Therefore:

$$I_p \propto P_{in} \quad (3.7)$$

When two frequencies, ω_1 and ω_2 , beat together on a photodetector, examining photodetector PD 1 first (Y path), and knowing that:

$$\begin{aligned} \sin u \sin v &= \frac{1}{2}[\cos(u - v) - \cos(u + v)] \\ \sin^2 u &= \frac{1}{2}(1 - \cos 2u) \end{aligned} \quad (3.8)$$

and:

$$\Delta\omega = |\omega_1 - \omega_2| \quad (3.9)$$

$$\Delta\phi = \phi_1 - \phi_2$$

$$Power \propto (amplitude)^2 \quad (3.10)$$

therefore from Equation (3.7), we can easily obtain:

$$\begin{aligned}
Y_3 &\propto [Y_2]^2 & (3.11) \\
&= \{E_{01} \sin[\omega_1(t - \Delta t) - \phi_1] + E_{02} \sin[\omega_2(t - \Delta t) - \phi_2]\}^2 \\
&= E_{01}^2 \sin^2[\omega_1(t - \Delta t) - \phi_1] + E_{02}^2 \sin^2[\omega_2(t - \Delta t) - \phi_2] \\
&\quad + 2E_{01}E_{02} \sin[\omega_1(t - \Delta t) - \phi_1] \sin[\omega_2(t - \Delta t) - \phi_2] \\
&= \frac{1}{2}E_{01}^2 \{1 - \cos[2\omega_1(t - \Delta t) - 2\phi_1]\} + \frac{1}{2}E_{02}^2 \{1 - \cos[2\omega_2(t - \Delta t) - 2\phi_2]\} \\
&\quad + E_{01}E_{02} \{\cos[\Delta\omega(t - \Delta t) - \Delta\phi] - \cos[(\omega_1 + \omega_2)(t - \Delta t) - (\phi_1 - \phi_2)]\}
\end{aligned}$$

Due to the low pass frequency response of the photo detector, frequencies higher than 20 GHz are filtered out. Frequency terms ω_1 , ω_2 , and $\omega_1 + \omega_2$ which are in the THz range, are filtered off by the photodetector. Therefore,

$$Y_3 \propto \left(\frac{1}{2}E_{01}^2 + \frac{1}{2}E_{02}^2\right) + E_{01}E_{02} \cos[\Delta\omega(t - \Delta t) - \Delta\phi] \quad (3.12)$$

If we assume photodetector frequency response as R_{DC} and R_{AC} corresponding to DC and AC signals respectively; I_{DC} and I_{AC} are the DC current output and the peak-to-peak AC current output of the photodetector, respectively:

$$I_{DC} = R_{DC} \left(\frac{1}{2}E_{01}^2 + \frac{1}{2}E_{02}^2\right) \quad (3.13)$$

$$I_{AC} = R_{AC} E_{01} E_{02}$$

Therefore:

$$Y_3 \cong I_{DC} + I_{AC} \cos[\Delta\omega(t - \Delta t) - \Delta\phi] \quad (3.14)$$

Similarly, for the photodetector in the X path (PD 2), one has:

$$\begin{aligned}
 X_2 &\propto [X_1]^2 & (3.15) \\
 &= \{E_{01} \sin[\omega_1 t - \phi_1 + \phi_a + \frac{\pi}{2}] + E_{02} \sin[\omega_2 t - \phi_2 + \phi_b + \frac{\pi}{2}]\}^2 \\
 &= \frac{1}{2} E_{01}^2 \{1 - \cos[2\omega_1 t - 2\phi_1 + 2\phi_a + \pi]\} + \frac{1}{2} E_{02}^2 \{1 - \cos[2\omega_2 t - 2\phi_2 + 2\phi_b + \pi]\} \\
 &\quad + E_{01} E_{02} \{\cos[\Delta\omega t - \Delta\phi + (\phi_a - \phi_b)] - \cos[(\omega_1 + \omega_2)t - (\phi_1 - \phi_2) + (\phi_a + \phi_b) + \pi]\}
 \end{aligned}$$

Again, as the detector filters off frequencies higher than 20 GHz, we have:

$$X_2 \propto \frac{1}{2}(E_{01}^2 + \frac{1}{2}E_{02}^2) + E_{01}E_{02} \cos[\Delta\omega t - \Delta\phi + (\phi_a - \phi_b)] \quad (3.16)$$

and:

$$I_{DC} = R_{DC}(\frac{1}{2}E_{01}^2 + \frac{1}{2}E_{02}^2) \quad (3.17)$$

$$I_{AC} = R_{AC}E_{01}E_{02}$$

Finally:

$$X_2 \cong I_{DC} + I_{AC} \cos[\Delta\omega t - \Delta\phi + (\phi_a - \phi_b)] \quad (3.18)$$

3.4 Mixer

The mixer [27] is also called the phase comparator, and is commonly used in RF (radio frequency) systems for frequency conversion. In Figure 3.5, the voltage at the secondary side of the LO transformer causes currents to flow through diode

pair D1 and D2 or D3 and D4, depending on the voltage polarity. The DC voltage at B (or C) is held at virtual ground potential ($V=0$) by the voltage divider action of the conducting diode pair. The diode pairs (D1, D2) and (D3, D4) alternate conduction, causing the ends of the RF transformer's secondary winding (B and C) to be alternately at ground potential, switching at a rate equal to the frequency of the input signal to the LO port. The instantaneous voltage at the IF port is determined by: 1) the level and polarity of the instantaneous voltage at the RF transformer's secondary winding; and 2) which terminal of the secondary is at ground potential at that instant. The output at the IF port contains the sum and difference of the frequencies of the signals input to the LO and RF ports. If the RF and LO signals have identical frequencies, then their frequency difference is zero (DC) which is the desired output for a phase detector. Their sum, which is at twice the input frequency, can be selectively filtered out if it is not already beyond the frequency response of the IF port.

By the identity:

$$\cos u \cos v = \frac{1}{2} [\cos (u + v) + \cos (u - v)] \quad (3.19)$$

The V_{IF} can be expressed as [28]:

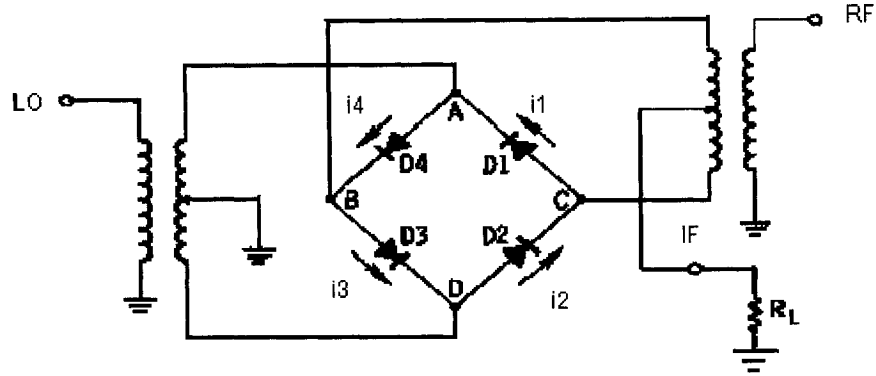


Figure 3.5: Double balanced four-diode ring mixer [27]. LO: local oscillation; IF: intermediate frequency; RF: radio frequency; D: diode.

$$\begin{aligned}
 V_{IF} &= V_{RF} \cos(\omega_{RF}t + \phi_{RF}) \left[\frac{4}{\pi} \sum_{n=1,3,5,\dots} \frac{1}{n} \cos(n\omega_{LO}t + \phi_{LO}) \right] \quad (3.20) \\
 &= V_{RF} \frac{4}{\pi} \left\{ \frac{1}{2} [\cos(\omega_{LO}t + \omega_{RF}t + \phi_{LO} + \phi_{RF}) + \cos(\omega_{LO}t - \omega_{RF}t + \phi_{LO} - \phi_{RF})] \right. \\
 &\quad \left. + \frac{1}{6} [\cos(3\omega_{LO}t + \omega_{RF}t + 3\phi_{LO} + \phi_{RF}) + \cos(3\omega_{LO}t + \omega_{RF}t + 3\phi_{LO} - \phi_{RF})] \right. \\
 &\quad \left. + \dots \right\}
 \end{aligned}$$

or ignoring the higher order terms ($\geq \omega_{LO}$ or ω_{RF}), it can be simplified as:

$$\begin{aligned}
 V_{OUT} &= \frac{2}{\pi} V_{RF} \cos[(\omega_{LO}t - \omega_{RF}t + \phi_{LO} - \phi_{RF})t] \quad (3.21) \\
 &= \frac{2}{\pi} V_{RF} \cos(\omega't + \phi_{LO} - \phi_{RF})
 \end{aligned}$$

where $\omega' = \omega_{LO} - \omega_{RF}$.

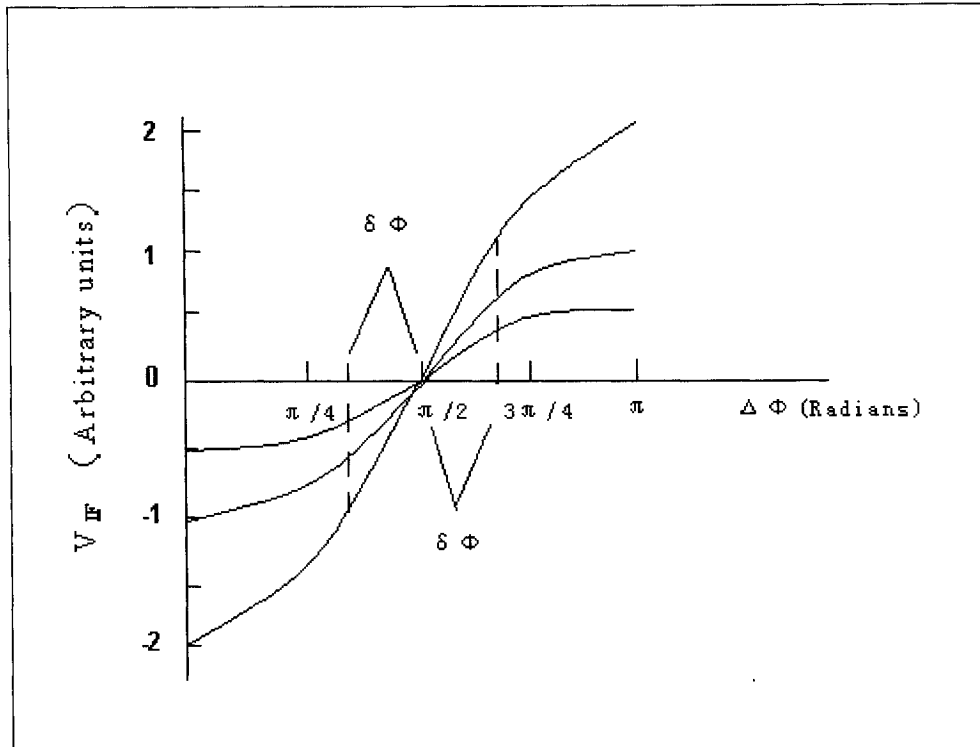


Figure 3.6: Typical phase detector response [28].

Figure 3.6 shows how the typical phase detector response curve [28] varies as $\cos(\Delta\phi + \pi)$, where $\Delta\phi = (\omega_{LO} - \omega_{RF})t$. Detector response is fairly linear over $\Delta\phi = \frac{\pi}{2} \pm \delta\phi$. The range of linear response depends on how much deviation from linearity can be tolerated. For example, if a 10% deviation from linearity is acceptable, then the linear response region will extend approximately from $\Delta\phi = \frac{\pi}{4}$ to $\frac{3\pi}{4}$, i.e., $\delta\phi = \pm\frac{\pi}{4}$. A Marki Microwave's M8-0420 double-balanced mixer was chosen in our setup. It offers broad RF/LO bandwidths (4 - 20 GHz) and a DC IF response (0 - 2 GHz) along with three SMA connectors.

In our setup, when two signals, X_2 and Y_3 , with identical frequency and constant amplitude are applied into the mixer, the result is a DC output voltage

proportional to the phase difference between these two signals. The phase difference $\Delta\omega\Delta t$ is the product of the frequency difference between the two lasers and the time difference between the signals Y_3 and X_2 . Thus we have:

$$\begin{aligned}
V_{OUT} &= \frac{2}{\pi} V_{RF} \cos[(\omega_{LO}t + \phi_{LO}) - (\omega_{RF}t + \phi_{RF})] & (3.22) \\
&= \frac{2}{\pi} R I_{AC} \cos\{[\Delta\omega(t - \Delta t) - \Delta\phi] - [\Delta\omega t - \Delta\phi + (\phi_a - \phi_b) + \phi_c]\} \\
&= \frac{2}{\pi} R I_{AC} \cos[\Delta\omega\Delta t + (\phi_a - \phi_b + \phi_c)]
\end{aligned}$$

where R is the output impedance of the photodetector, and ϕ_c is the microwave phase difference induced by the electrical cable length difference for X_2 and Y_3 .

If we define V_{PP} is the peak-to-peak voltage output of the mixer, where $V_{PP}(\Delta\omega, P_L, P_R) = \frac{2}{\pi} R I_{AC}$, then we have:

$$V_{OUT} = V_{PP}(\Delta\omega, P_L, P_R) \cdot \cos[\Delta\omega\Delta t + (\phi_a - \phi_b + \phi_c)] \quad (3.23)$$

Now, let us analyze two different cases:

Case 1 — Lock V_{OUT} using the feedback circuit, then $[\Delta\omega\Delta t + (\phi_a - \phi_b)]$ is locked too (ϕ_c is constant). By tuning Δt , then $\Delta\omega$ changes over a certain range.

Case 2 — Once the system is locked and also with Δt fixed, if the laser carrier frequency has a small fluctuation $\delta\omega$, then using the relation $\Delta\omega = \delta\omega + \Delta W$, we may separate phase ($\Delta\omega\Delta t$) into two components: a phase error term ($\delta\omega\Delta t$) and a phase offset term ($\Delta W\Delta t$).

$$V_{OUT} = V_{PP}(\Delta\omega, P_L, P_R) \cdot \cos[\delta\omega\Delta t + \Delta W\Delta t + (\phi_a - \phi_b + \phi_c)] \quad (3.24)$$

Since the mixer has a relatively flat frequency response, the following is valid:

$$V_{PP}(\Delta\omega, P_L, P_R) \cong V_{PP}(\Delta W, P_L, P_R) \quad (3.25)$$

Therefore, rewrite V_{OUT} as follows:

$$\begin{aligned} V_{OUT} &= V_{PP}(\Delta W, P_L, P_R) \cdot \cos\{\delta\omega\Delta t + [\Delta W\Delta t + (\phi_a - \phi_b + \phi_c)]\} \quad (3.26) \\ &= V_{PP}(\Delta W, P_L, P_R) \cdot \{\cos(\delta\omega\Delta t) \cos[\Delta W\Delta t + (\phi_a - \phi_b + \phi_c)] \\ &\quad - \sin(\delta\omega\Delta t) \sin[\Delta W\Delta t + (\phi_a - \phi_b + \phi_c)]\} \end{aligned}$$

Now set

$$\Delta W\Delta t + (\phi_a - \phi_b + \phi_c) = \frac{\pi}{2} \quad (3.27)$$

Using the condition that $\delta\omega$ is very small, this implies that:

$$\begin{aligned} V_{OUT} &= -V_{PP}(\Delta W, P_L, P_R) \cdot \sin(\delta\omega\Delta t) \quad (3.28) \\ &= -V_{PP}(\Delta W, P_L, P_R) \cdot \delta\omega\Delta t \end{aligned}$$

Thus, there is an almost linear proportional relationship:

$$V_{OUT} \propto -\delta\omega \quad (3.29)$$

This relationship can be used to provide the compensation information for the feedback circuit which will now be discussed.

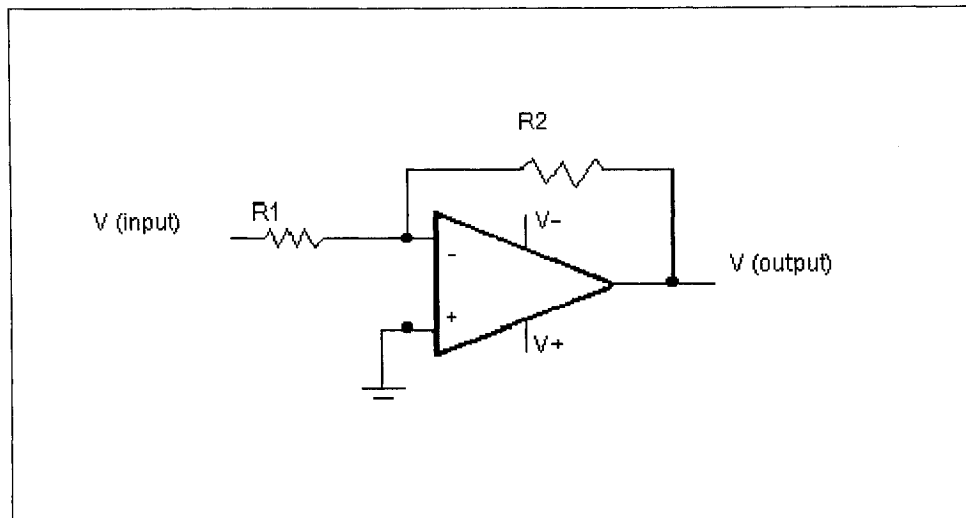


Figure 3.7: Inverting amplifier: $V_{out} = -\frac{R_2}{R_1} V_{in}$ (p control).

3.5 Feedback Circuit

The operational amplifier (OA) can be set up as an inverting amplifier, refer to Figure 3.7 for the circuit. This configuration is a basic feedback circuit. There are several feedback designs: proportional control (P control), proportional derivative control (PD control), proportional integrating control (PI control), and proportional integral derivative control (PID control). P and PI control are the most commonly used. A proportional controller [Figure 3.7] has a characteristically fast rise time. An integral control [Figure 3.8] has the advantage of eliminating steady-state error. In this work, a PI control was built to provide the feedback signal to the current input of the DFB lasers.

The feedback loop used in the system [Figure 3.9] reveals three parts:

Part 1 ($G_1(j\omega)$) is the laser tuning section. From the specification sheet of the

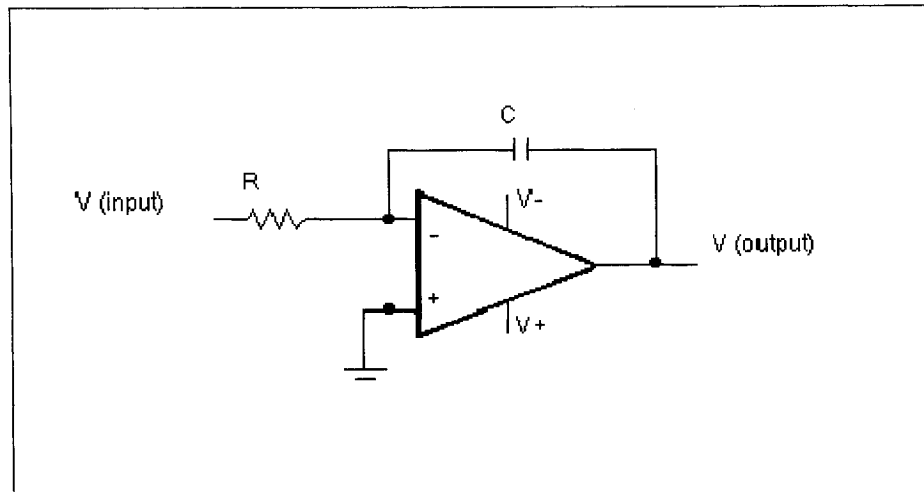


Figure 3.8: Integration circuit: $V_{out}(t) = \frac{1}{RC} \int_0^t V_{in}(t)dt + V_{out}(t = 0)$.

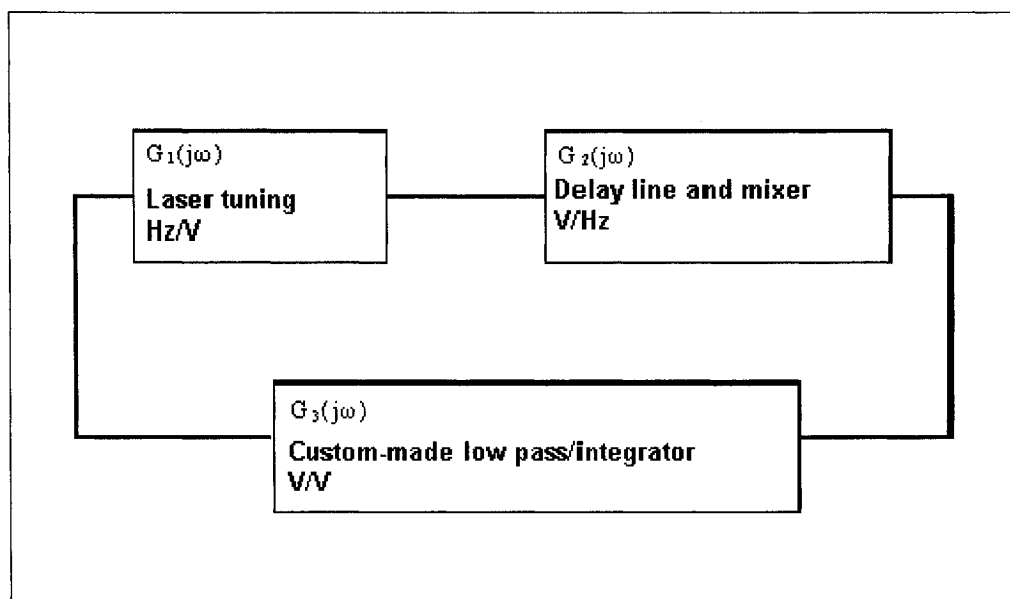


Figure 3.9: Block diagram for stabilizing the laser frequency.

DFB lasers, the current source has a tuning transfer function of 100 mA/V in the 0 - 200 mA range. A measurement of the transfer function between an applied voltage modulation and a resulting frequency output was performed, refer to results in the table below: [MF—Modulation Frequency(Hz); BF —Beat Frequency (MHz)]

MF	0.02	10	50	100	1000	2k	5k	10k	20k	50k	100k
BF	1800	1600	1550	1550	1500	1350	1200	1000	850	600	450

The modulation amplitude was set at 20 mV_{p-p}. The shift for the laser was about 1550 MHz/20mV_{p-p}=77.5×10⁹Hz/V at low frequency. It dropped to 0.707 of the maximum at roughly 10 kHz when the time constant measured is RC=1.59×10⁻⁵ s. Thus, the transfer function for the laser in converting voltage modulation into frequency modulation is given as:

$$G_1(j\omega) = \frac{7.75 \times 10^{10}}{1 + j\omega(1.59 \times 10^{-5})} (\text{Hz/V}) \quad (3.30)$$

The second part ($G_2(j\omega)$) is the delay line and mixer section. The delay time and power to the mixer were adjusted to give a response as seen in Figure 3.10: the slope was 100(mV)/250(MHz)=4.0×10⁻¹⁰ (V/Hz) as determined by experimental measurements. Thus, we have:

$$G_2(j\omega) = 4.0 \times 10^{-10} (\text{V/Hz}) \quad (3.31)$$

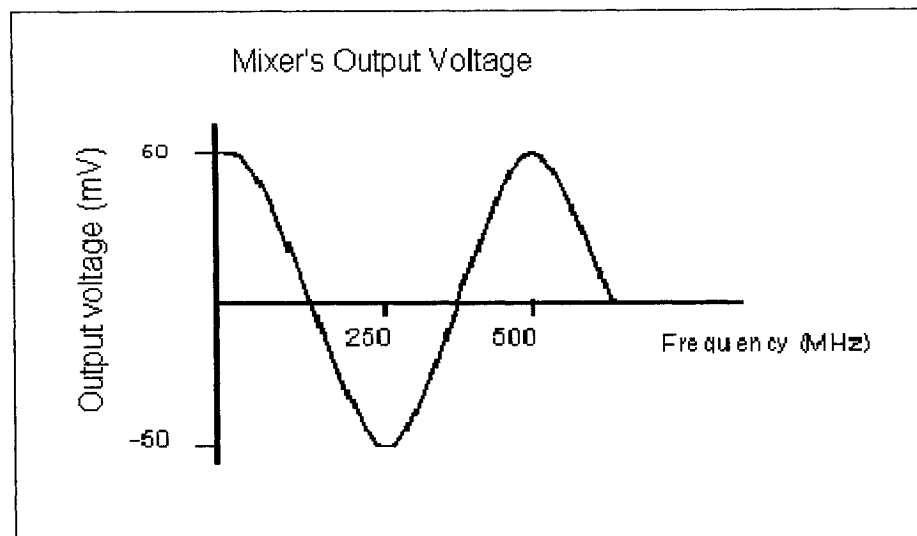


Figure 3.10: Mixer's output voltage vs. frequency.

Third part, $G_3(j\omega)$ is the home-made PI Control circuit; shown in Figure 3.11. Several band-pass filters are used to filter out noise. This circuit was initially built in NRC (National Research Council, Canada) by Mr. John Bernard.

After applying the PI circuit, one finds that the beat note is stabilized (shown in Figure 3.12) as opposed to the unstable beat note shown in Figure 3.2 with no feedback, and also it is tunable.

With the two stable frequency-locked lasers, we next built the sensor system. The details are described in the following chapter

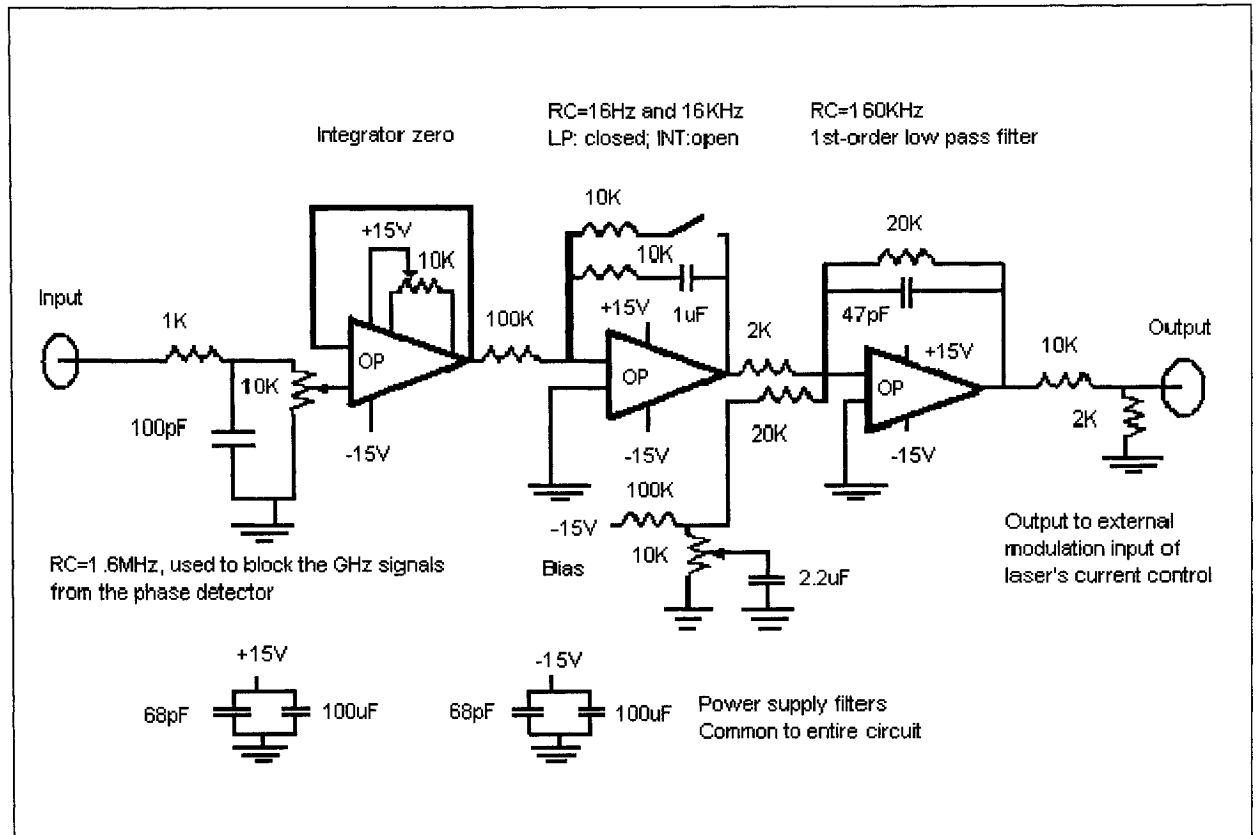


Figure 3.11: The PI control feedback circuit. OP: operational amplifier.

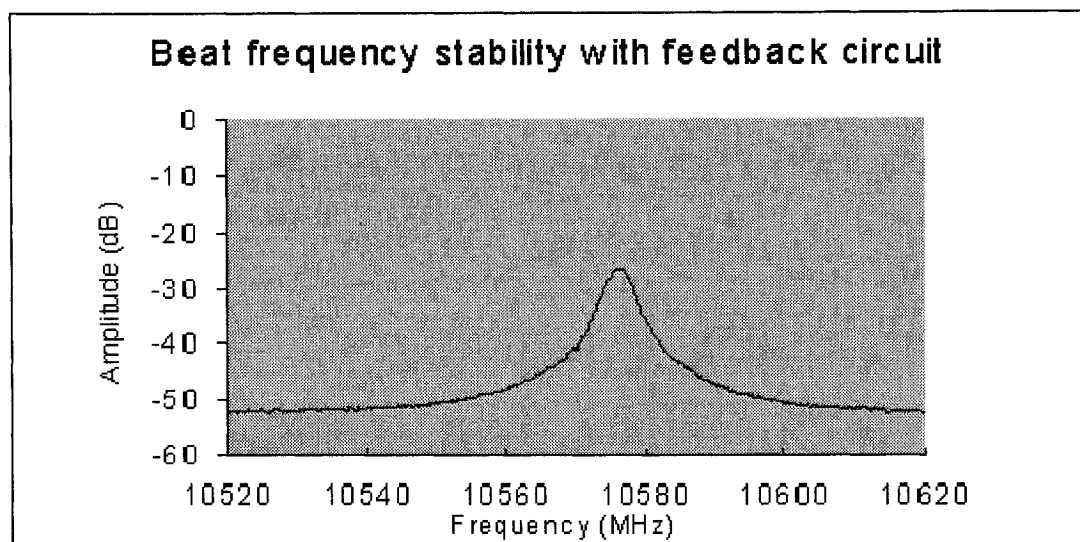


Figure 3.12: Beat signal with feedback. Beat frequency is stable with the feedback circuit.

CHAPTER 4
DISTRIBUTED FIBER OPTIC SENSOR SYSTEM BASED ON TWO
DISTRIBUTED FEEDBACK LASERS

4.1 System Configuration

In the last chapter, we showed that the offset locking technique could be used to stabilize two DFB lasers at the offset frequency. Two DFB lasers (close together in frequency) produce a beat signal, which is equally divided into two parts. By comparing the phase difference of these two beams (often one beam passes through an optical delay line) and using this difference to provide a feedback signal to the current source of one of the lasers, the frequency of laser follows that of the other laser resulting in a stabilized beat signal. By tuning the optical delay line, we can change the beat frequency within a certain range. The Brillouin frequency for 1554 nm light is 10860 MHz. Two lasers can be locked at this offset frequency with a 925 MHz tuning range.

Figure 4.1 shows a block diagram of our system. One of the DFB lasers (pump) launches a CW pump beam, while the other DFB laser (probe) is modulated by an electro-optic modulator (EOM) to produce a pulsed beam (Stokes probe). The two beams are launched into the fiber under test at the opposite ends of the fiber. Due to Brillouin amplification, the Stokes wave is continually amplified as it travels through the sensing fiber; the resulting depletion in the CW pump power is measured over a range of frequency differences to create the Brillouin loss spectrum.

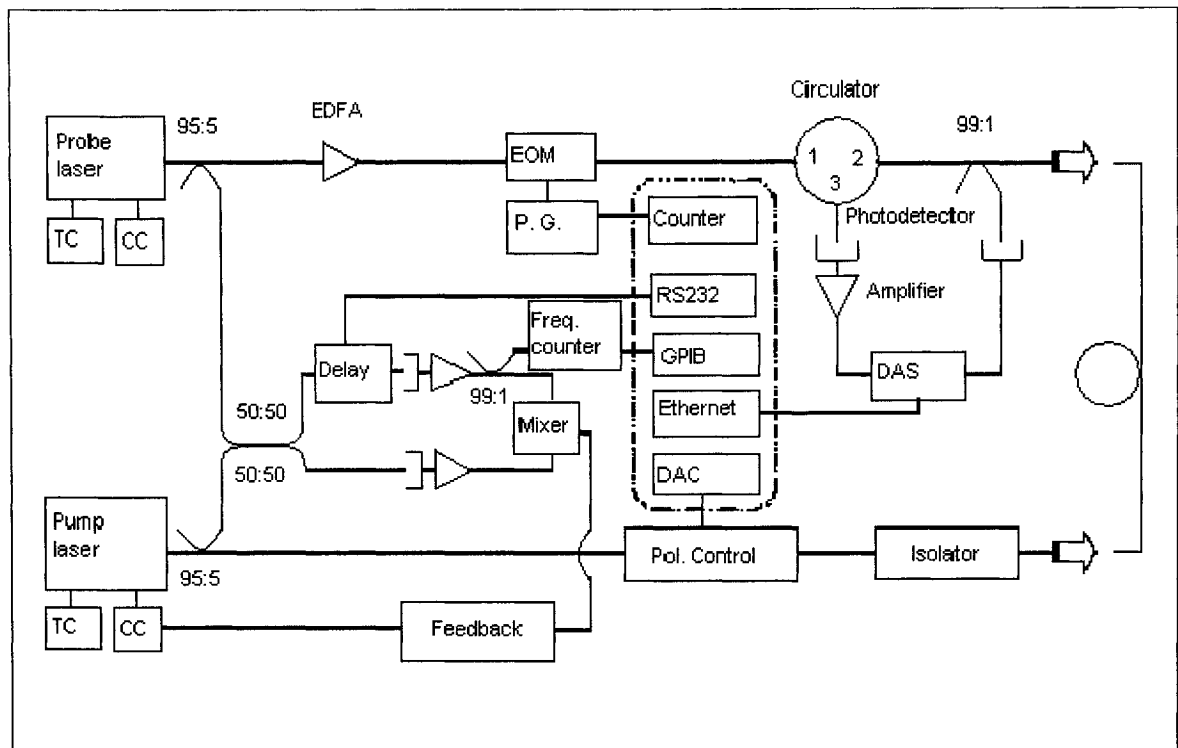


Figure 4.1: The 1550 nm sensor system setup. TC: temperature control; CC: current control; PG: pulse generator; DAC: digital to analog converter; DAS: data acquisition system; Pol. Control: polarization control.

Therefore, the Brillouin loss spectrum and Brillouin spectrum (spectral profile) are complementary. The use of a pulsed probe beam allows the system to acquire the Brillouin loss spectrum in any position along the fiber under test. Therefore, a 3-D data set in position (time), frequency and power (loss) is collected. With analysis, we obtain time-domain Brillouin scattering signals and Brillouin loss spectrums at any location along the fiber. The circulator and isolator used in the system play an important role in stopping lights going back to the laser cavities.

Recall that the Brillouin shift depends on the effective refractive index of the fiber, and thus it changes whenever the refractive index of the silica changes in response to any local environmental variations (such as temperature and strain). By monitoring the Brillouin frequency shift along the fiber, one can successfully map out the distribution of temperature or strain. When temperature stays constant, the strain information can be obtained from Brillouin frequency shift.

Some of the important optical and electro-optic components used in our system are listed in the following sections.

4.2 Electro-Optic Modulation

We use an electro-optic modulator driven by a pulse generator to modulate one of the CW lasers to produce successive pulses that are launched into one side of the fiber under test, thus allowing us to obtain distributed information along the fiber. The EOM is a very critical component in our distributed sensor system.

The EOM is made from lithium niobate (LiNbO_3) which has low optical loss and a high electro-optic coefficient. The electric-optical coefficient relates the re-

fractive index of the material changes in response to an applied electric field – thus one can change the speed of light passing through this medium by applying a voltage.

Figure 4.2 gives a block diagram of a typical modulator. The input light enters the modulator and then splits into two paths using an optical beam-splitter. The upper optical path passes through a length of LiNbO_3 crystal. Light in the lower path experiences a fixed time delay. After the light travels through these two separate paths an optical combiner (beam-splitter) merges the two beams, and thereafter the light travels on one path. By applying an electric field to the crystal, the material refractive index changes and thus we have a variable time delay. If the time delay through the fixed fiber (lower path) and the LiNbO_3 crystal (upper path) is equal, the two signals will be in phase (constructive interference) and result in maximum output when they reach the output optical combiner. When the applied electric field changes the refractive index in the crystal to delay the light by half of one wavelength, the two light signals will be out of phase (destructive interference) and result in minimum output.

In this experiment, a JDS Uniphase Corporation manufactured OC-192, 10 GHz modulator is driven by an Avtech Electro Systems' pulse generator (model: AVMP). The pulse generator can produce an amplitude-adjustable pulse with a 5 - 100 ns pulse-width and is triggered by a function generator. For a 2 km fiber, the repetition rate is set to 20 kHz to make sure there is one pulse in the fiber for distributed sensors, and the pulse-width is 50 ns.

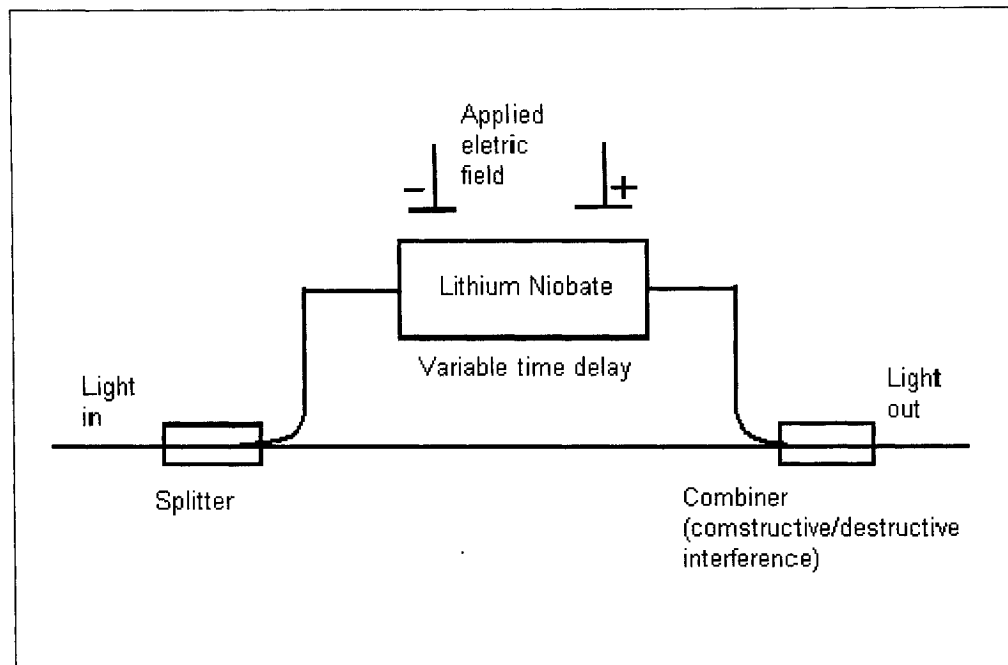


Figure 4.2: Typical Lithium Niobate (LiNbO_3) optical modulator [29].

4.3 Polarization Scrambler

According to research done by M. Deventer in 1994 [13], the Brillouin gain differs depending on whether the two beams have identical polarizations or orthogonal polarizations. To overcome the polarization dependence of the Brillouin gain, polarization control (scrambling or depolarization) of the pump beam is required [30]. This is the reason that a General Photonics Corporation's PolarITEIII dynamic polarization controller is used to scramble the polarization states of the CW pump beam (see Figure 4.3). This polarization scrambler actively changes the state of polarization by squeezing the fiber to induce a large birefringence via the photo-elastic effect [31]. With the photo-elastic effect, an acoustic wave propagating through an acousto-optic material creates periodic changes in the refractive

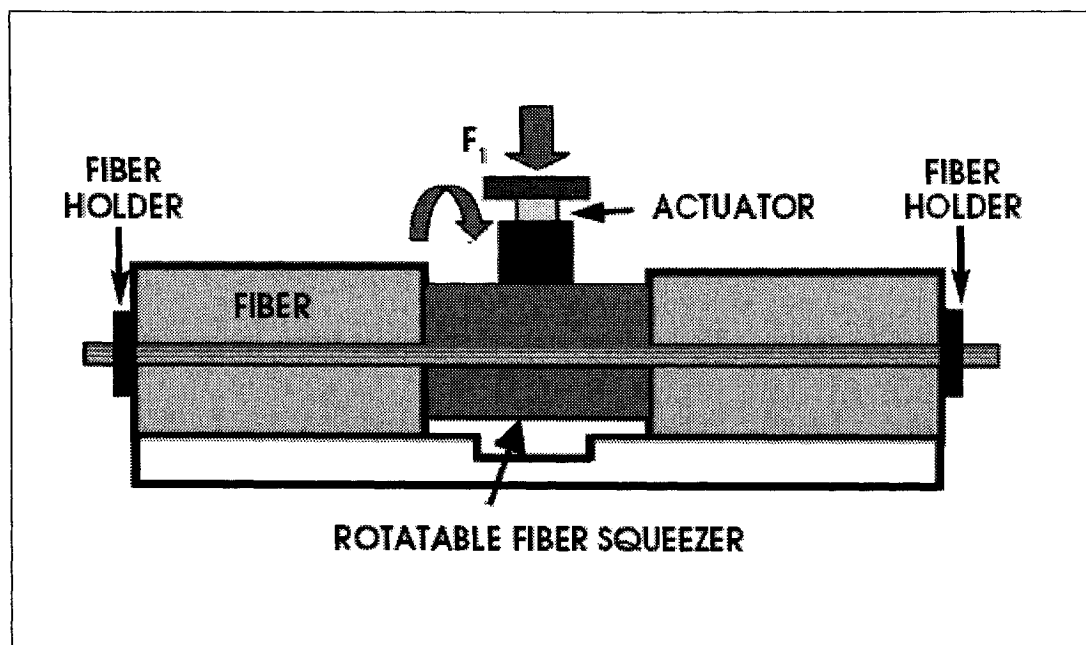


Figure 4.3: Polarization control with a single wave plate with variable retardation and orientation. Shown here is an all-fiber approach with rotatable fiber squeezer [31].

index [[26], page 343]. The effect works over a frequency range of 10 Hz to 12.5 kHz.

4.4 Experimental Results

Compare the beat signal with feedback operation to the signal without feedback operation in Figures 3.12 and 3.2. With feedback operation, the standard deviation of the beat frequency (at 10860 MHz) is 20 kHz over 10 minutes shown in Figure 4.4. 10 minutes is enough for a Brillouin spectrum scanning in our setup. The standard deviation is the most commonly used measure of spread. It is the square root of

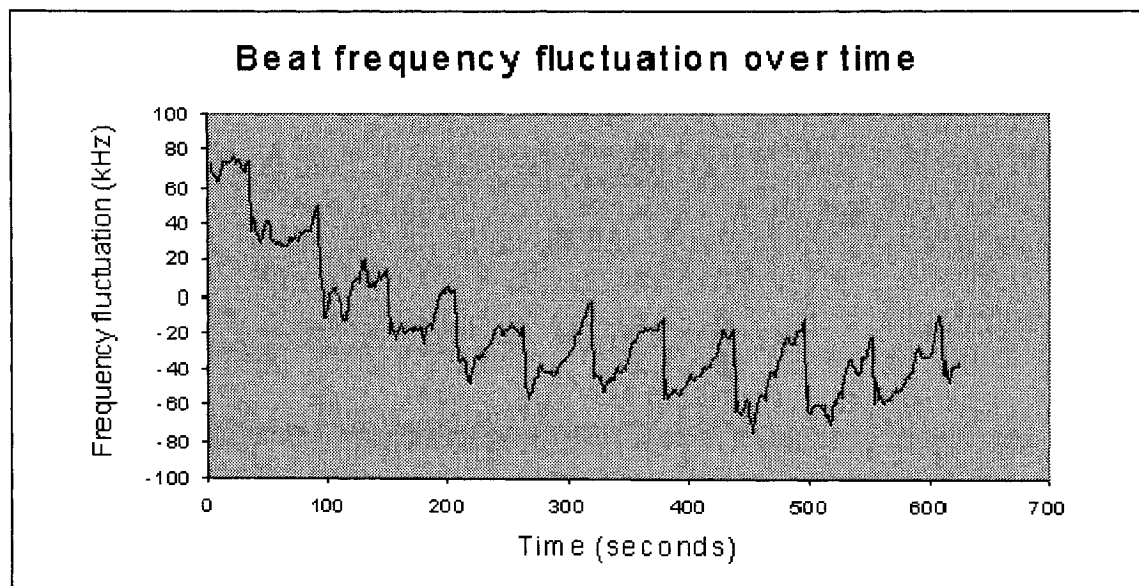


Figure 4.4: Beat frequency stability. 20 kHz for standard deviation in 10 minutes.

the variance, and the variance is computed as the average squared deviation of each number from its mean. In Figure 4.5, we demonstrate a 925 MHz continuous tuning range around the 10860 MHz Brillouin frequency by using an optical delay line.

Figure 4.6 shows a time-domain Brillouin scattering signal measured at the Brillouin frequency 10860 MHz for a 1.8 km single mode fiber with 2000 signals averaged. An average of 1000, 2000, or even more signals is taken to reduce the noise. The pulse width is set to 50 ns equivalent to 5 m spatial resolution. The pulse repetition rate is 20 kHz since 20 kHz corresponds to 50 μ s during which the pulsed light can travel 20 km (i.e. pulse leaves fiber before next pulse is generated). This time domain diagram records the intensity of the pump power as a function of

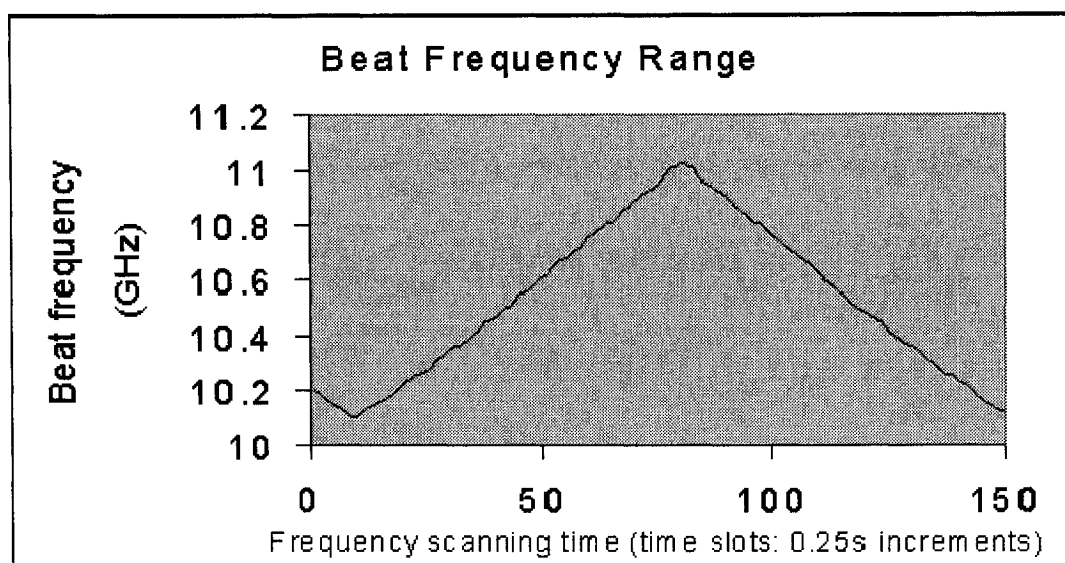


Figure 4.5: The tuning of beat frequency. 925 MHz is achieved by tuning optical delay line.

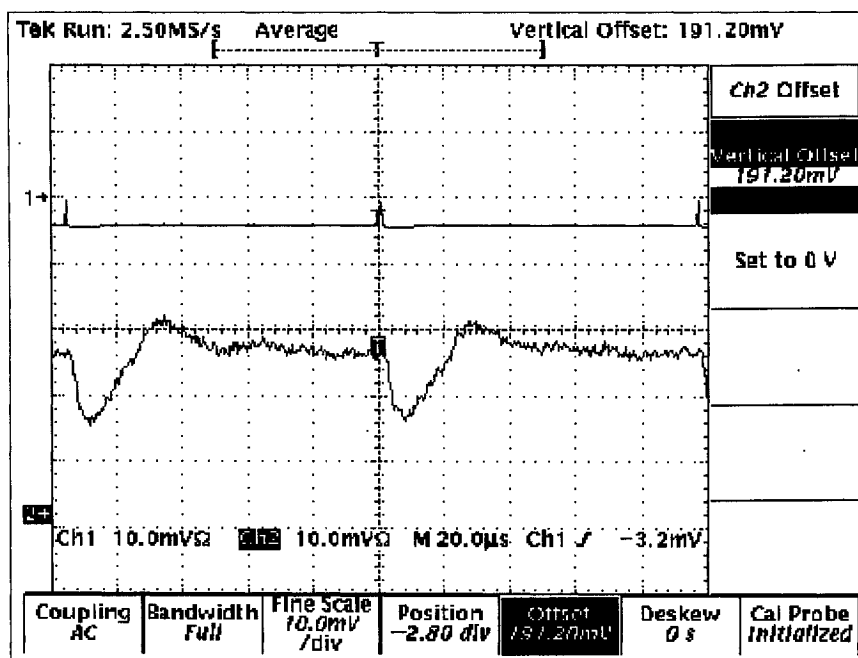


Figure 4.6: Time domain signal for a 1.8 km long fiber (measured by OTDR). The vertical scale is mV (voltage) and the horizontal scales is $20 \mu s$ (time) . Channel 1 is the pulse produced by EOM and it is sent into the fiber under test. Channel 2 is the CW beam received after travelling through the fiber under test.

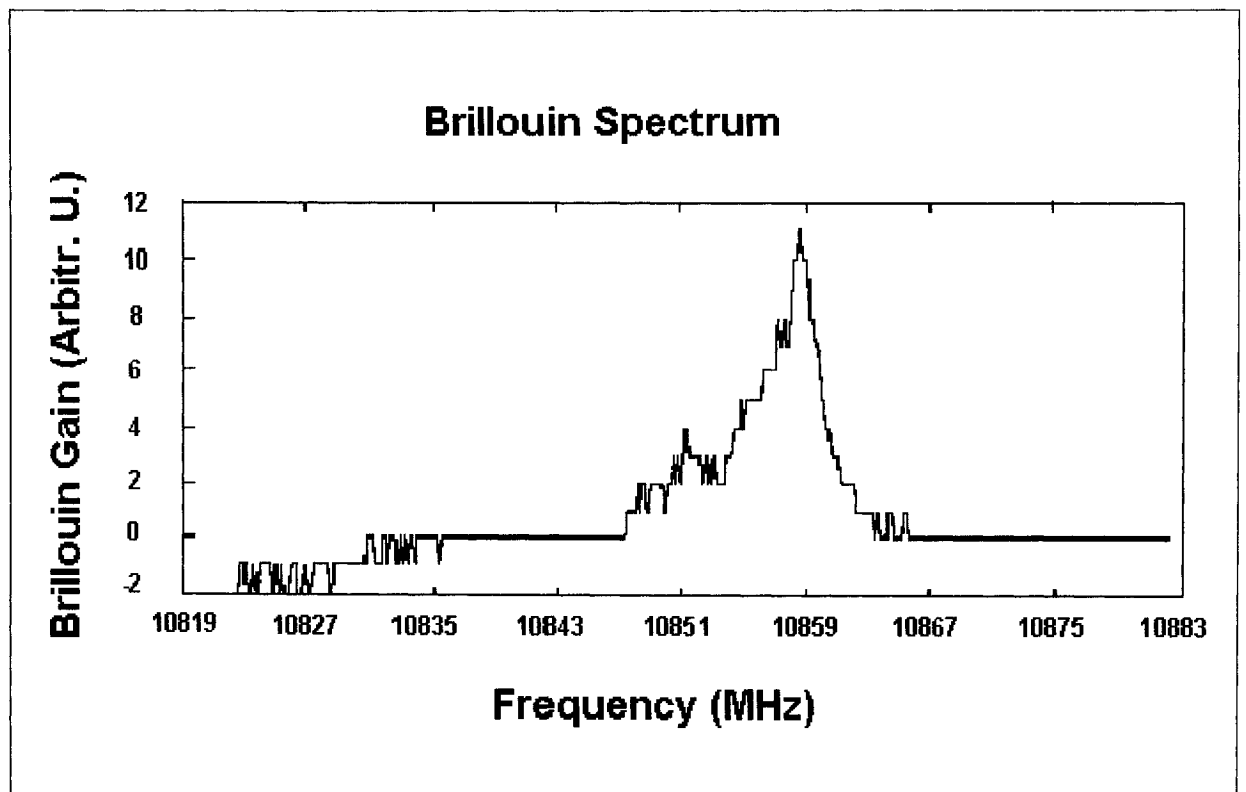


Figure 4.7: Brillouin gain spectrum at the center of the 1.8 km fiber. The peak frequency is located at 10857 MHz.

time (can convert to distance) from when the pulse first enters the fiber to when it exits the fiber at the far end. Figure 4.7 is the Brillouin spectrum at the center of the 1.8 km fiber. As can be seen, the peak signal (10857 MHz) corresponds to the Brillouin frequency of 10860 MHz with a 3 MHz variation at room temperature. The signal-to-noise ratio (SNR) for this spectrum is about 15 dB. Initially, it was thought that this low SNR could be caused by the broad linewidth of the DFB laser which is about 1000 times larger than the stabilized Nd:YAG laser's linewidth (SNR for Nd:YAG laser sensor system is 10 - 20 dB higher). In the next section, the Brillouin gain is simulated with this broad spectral width and it is found that the linewidth is not the major factor for the low SNR.

4.5 Simulation of Brillouin Scattering

The stabilized Nd:YAG laser has a frequency bandwidth of 5 kHz/ms [32] as compared with the 5 MHz linewidth of a common DFB laser [25]. Using numerical simulation method, one can examine the effect of linewidth on the Brillouin gain/loss spectrum.

The coupled wave equations for the steady state Brillouin scattering are given by Equation 2.6.

The numerical solution for these coupled equations follows:

Assume the length of the fiber under test is $L\Delta z$, the location along the fiber where the spectrum is of our interest is given by $z = m\Delta z$, with Δz is the spatial resolution. We assume $\Delta z = 1m$, $m = 0, 1, 2 \dots L$ and $L = 1000$ in this simulation.

First, write a discrete recursive solution to obtain I_p^{m+1} and I_S^{m+1} in terms of

the m th values, where p represents pump and S represents Stokes:

$$\begin{aligned} I_p^{m+1} &= \Delta z \times (-\alpha I_p^m - g_B I_p^m I_S^m) + I_p^m \\ I_S^{m+1} &= \Delta z \times (\alpha I_S^m - g_B I_p^m I_S^m) + I_S^m \end{aligned} \quad (4.1)$$

Next, apply the input boundary conditions ($I_p^L = 0.020(\text{Watt})/[\pi \times \{5e^{-6}(\text{meter})\}]^2$) and $I_S^0 = 0.001(\text{Watt})/\{\pi \times [5e^{-6}(\text{meter})]^2\}$) to solve the coupled equations.

Dr. Bao et al. first suggested a numerical solution in 1995 [33], and in 1998 Dr. Bao and Dr. Chen [34] provided a correction to the solution provided in the classic text book "Nonlinear Fiber Optics" by Agrawal. Extending this work, we introduce the linewidth terms into the equations, to better simulate DFB laser based Brillouin scattering.

Referring to Figure 4.8, consider the incident light as a linear combination of many incident beams at different frequencies (dealing with intensities instead of fields here). Now, consider the linewidth of DFB lasers to be N times bigger than that of Nd:YAG lasers:

$$\begin{aligned} \frac{dI_p(z)}{dz} &= -\alpha \sum_{i=1}^N I_{p_i}(z) - \sum_{i=1}^N \sum_{j=1}^N g_{B_{ij}} I_{p_i}(z) I_{s_j}(z) \\ \frac{dI_s(z)}{dz} &= \alpha \sum_{j=1}^N I_{s_j}(z) - \sum_{i=1}^N \sum_{j=1}^N g_{B_{ij}} I_{p_i}(z) I_{s_j}(z) \end{aligned} \quad (4.2)$$

Next, using the numerical approximation method, and

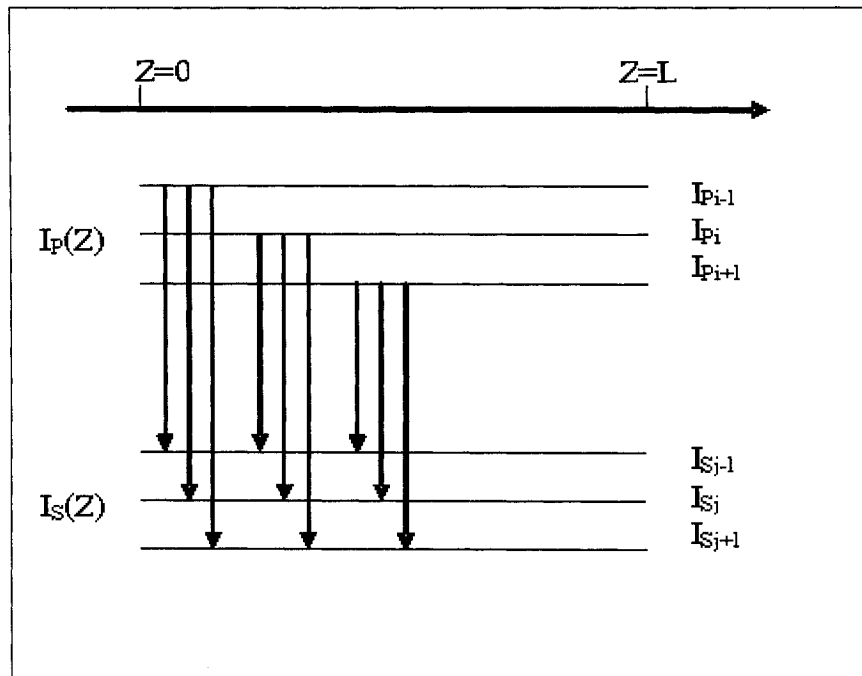


Figure 4.8: Assume the pump (I_p) and Stokes (I_s) have many transitions along fiber length L . Consider the incident light as a linear combination of many incident beams at different frequencies.

$$\sum_{i=1}^N I_{p_i}(z) = I_p$$

$$\sum_{j=1}^N I_{s_j}(z) = I_s$$

we have:

$$\frac{I_p^{m+1} - I_p^m}{\Delta z} = -\alpha I_p^m - \sum_{i=1}^N \sum_{j=1}^N g_{B_{ij}} I_{p_i}^m I_{s_j}^m \quad (4.3)$$

$$\frac{I_s^{m+1} - I_s^m}{\Delta z} = \alpha I_s^m - \sum_{i=1}^N \sum_{j=1}^N g_{B_{ij}} I_{p_i}^m I_{s_j}^m$$

where $N = \frac{\text{linewidth of DFB laser}}{\text{linewidth of Nd:YAG laser}} = \frac{5 \text{ (MHz)}}{5 \text{ (kHz)}} = 1000$.

The Brillouin gain spectrum can be treated as a Lorentzian distribution when the laser linewidth is much less than the natural linewidth of the phonon. Use $g_p \approx 5 \times 10^{-11} \text{ m/W}$ as the peak value of Brillouin gain ($\nu = \nu_B$) at the oscillation frequency with $\Gamma_B = \frac{1}{T_B} = \frac{1}{50 \text{ (ns)}} = 20 \text{ MHz}$ being the damping rate of the acoustic waves, and the peak Brillouin frequency is 10860 MHz.

Treat the laser beam using a Gaussian profile, thus the distribution function is:

$$I(\nu) = I_0 e^{-4 \ln 2 \left(\frac{\nu - \nu_B}{\delta \nu} \right)^2} \quad (4.4)$$

From the identity $\int_{-\infty}^{\infty} e^{-x^2/2} dx = \sqrt{2\pi}$, one may derive $I_0 = \frac{\sqrt{\pi} \ln 4}{\delta \nu} I_{total}$. Then the laser beam distribution is:

$$I(\nu) = \frac{\sqrt{\pi} \ln 4}{\delta \nu} I_{total} e^{-4 \ln 2 \left(\frac{\nu - \nu_B}{\delta \nu} \right)^2} \quad (4.5)$$

where the laser linewidth $\delta\nu = 5$ MHz, and I_{total} is the incident optical intensity.

Now, solve the above equations numerically (refer to code in Appendix C). The simulation results (Figures 4.9 and 4.10) show that the pump beam keeps losing the energy to the Stokes pulse along the fiber through the Brillouin scattering effect after being launched into the fiber. Meanwhile, the Stokes pulse keeps gaining power along the fiber from the interaction with CW pump beam (so called "Brillouin amplification"). The Stokes power starts to grow at its initial position of $Z = 20$ meters. The pump power starts to decrease at its initial position of $Z = 0$ meter. The full-width-half-maximum (FWHM) of the Brillouin spectrum for the DFB lasers (75MHz) does not have a big difference with that for the Nd:YAG lasers (90MHz). Therefore, the linewidth of the laser used does not affect the Brillouin spectrum. On the other hand, the stability of the laser frequency may be the critical parameter in the sensor system's performance. This could indicate that a 20 kHz frequency deviation over 10 minutes of average time is not sufficient to allow a 25 dB SNR for the Brillouin spectrum.

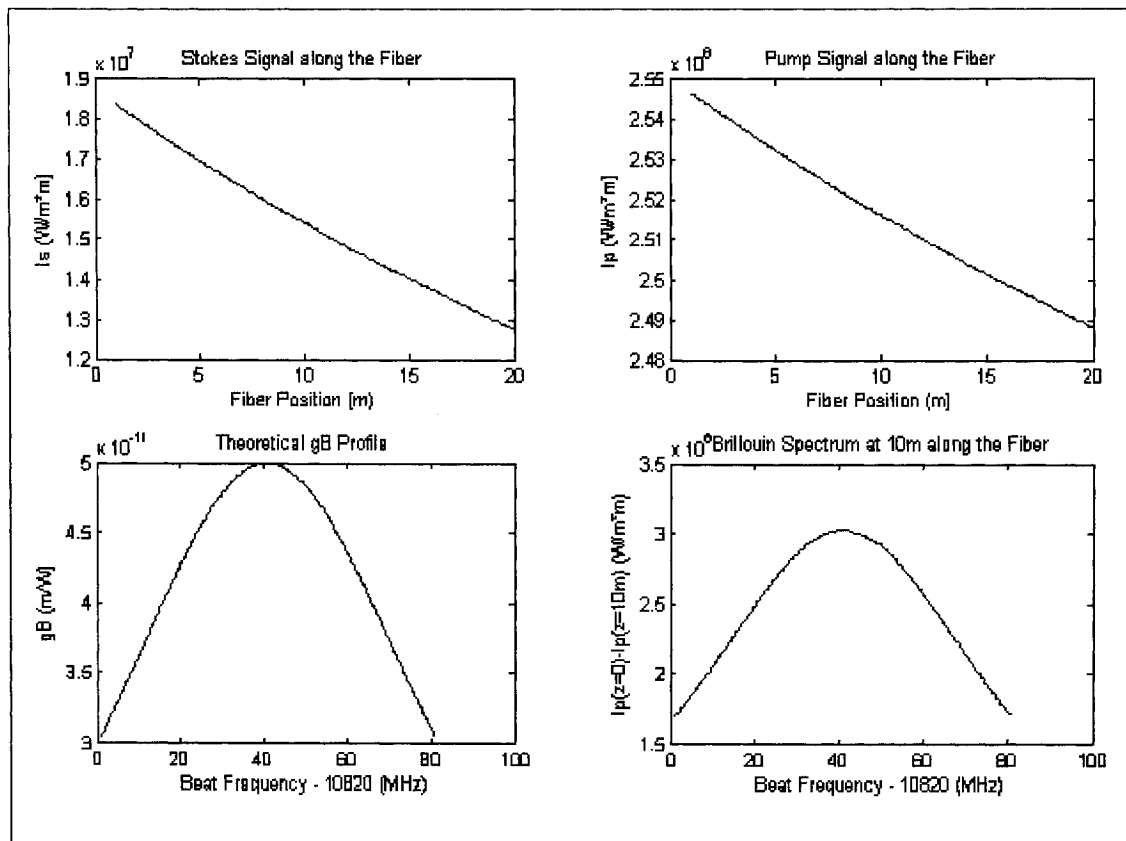


Figure 4.9: The laser's line-width is 5 kHz. The pulse width of the probe beam is 50 ns. Total fiber length is 20 m. The FWHM of the Brillouin spectrum is 90 MHz.

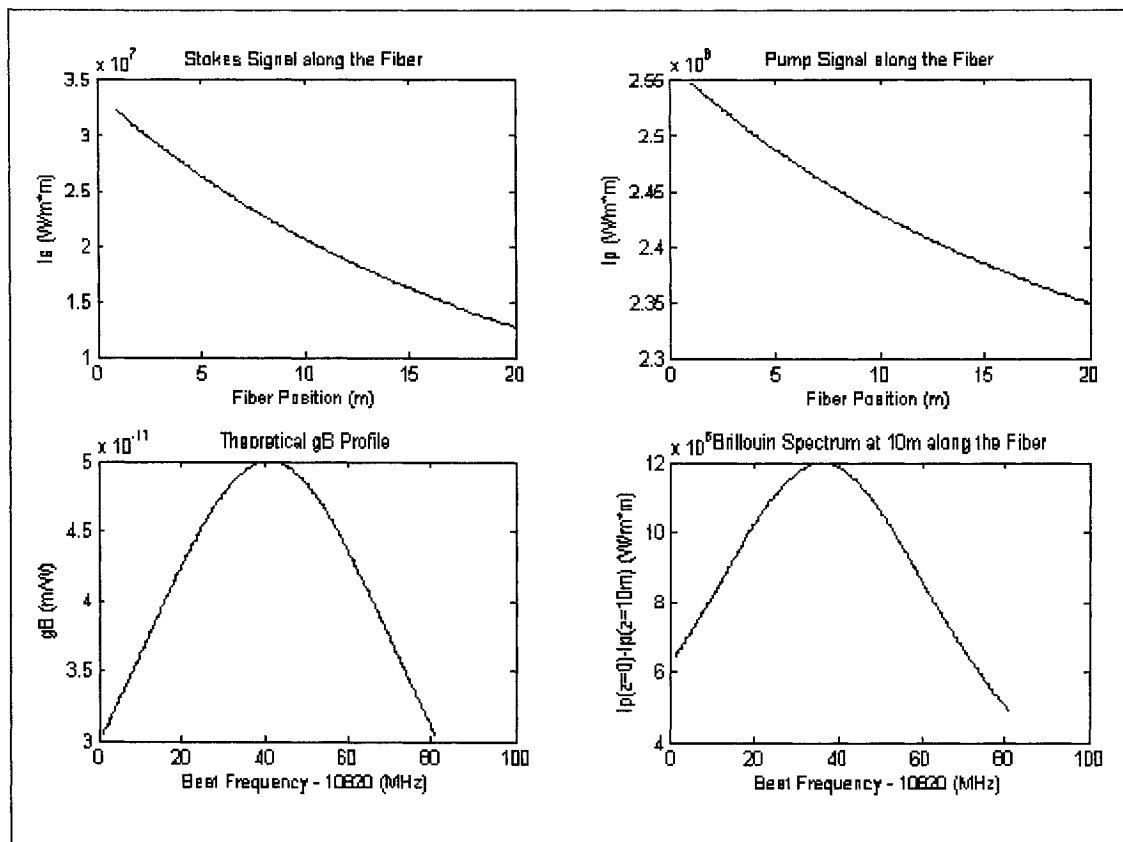


Figure 4.10: The laser's line-width is 5 MHz. The pulse width of the probe beam is 50 ns. Total fiber length is 20 m. The FWHM of the Brillouin spectrum is 75 MHz.

CHAPTER 5

CONCLUSION (PART I)

Over the past two years, this project has successfully applied the offset locking technique to stabilize the beat signal between two DFB semiconductor lasers and then used these laser sources to measure Brillouin loss spectrum. In the first year, the focus was on searching for two stable and tunable DFB light sources. The sensor system requires a frequency stability of less than 100 kHz over a millisecond time scale. Thus, two DFB lasers were offset-locked to achieve 100 kHz stability, but over a longer time period (10 minutes) of averaging. In addition, by applying an optical delay line, one could tune this beat frequency over a 900 MHz range. Then, in the following year, the whole sensor system was built using more than 20 optical, electrical and electro-optic components. The resulting time domain signal and frequency domain spectrum for a 1.8 km long fiber (SMF-28) were obtained. For a laser at 1554 nm, with a Corning SMF-28 optical fiber at room temperature, the Brillouin peak frequency is expected to be at 10860 MHz. The experimental result was very close at 10857 MHz. However, the SNR was only 15 dB for a 5 m spatial resolution, not as good as that of the stabilized Nd:YAG sensor system's over 25 dB SNR. The Brillouin scattering process was simulated under the condition that the DFB lasers have a much wider spectral width than that of the Nd:YAG lasers. The results showed that this did not affect the Brillouin spectrum. In future work, it is recommended that one improves the beat frequency stability of the DFB lasers

to a few kHz in order to increase the SNR of the sensor system.

Part II

STUDY OF POLARIZATION EFFECTS IN OPTICAL FIBERS

CHAPTER 6

BACKGROUND

Being a low cost medium for transmitting information over long distances, the optical fiber has played a very important role in the field of modern telecommunications in the past 20 years. In high speed fiber optic communications systems, polarization mode dispersion (PMD) and polarization dependent loss (PDL) are very critical effects which are harmful to the system data transmission rate above 10 Gb/s. Much research is under way to find better methods to compensate for these impairments in the communication system. For instance, the principal states of polarization (PSP's) [35] and their differential group delay (DGD) have been extensively studied to describe the polarization mode dispersion in single mode fibers. There are a number of techniques [36] [37] [38] [39] to measure the PMD. However most of these techniques have assumed that the system does not have any polarization dependent loss or gain (PDL/G). Although the Jones matrix eigenvalue analysis method by Heffner [38] does give a correct DGD value for a system with PDL/G, utilization of this method requires complete knowledge of both the input and output state of polarization (SOP) for three independent polarizations. The complex plane method introduced by Eyal et al.[39] requires the measurement of three output SOPs as well as their derivatives. Because of their unconventional representation, it is not straightforward to provide output complex PSP vector information. In a system with PMD and PDL/G, Gisin and Huttner [40] showed

that the PSP vector

$$\vec{W} = \vec{\Omega} + i\vec{\Lambda} \quad (6.1)$$

becomes complex. The normalized output state of polarization (SOP) described on the Poincaré sphere obeys the following equation of motion [40] [41] [42]:

$$\frac{d\vec{S}}{d\omega} = \vec{\Omega} \times \vec{S} - (\vec{\Lambda} \times \vec{S}) \times \vec{S} \quad (6.2)$$

where \vec{S} is the normalized Stokes vector, ω is the angular frequency of the light, and $\vec{\Omega}$ is the real part of the complex PSP vector \vec{W} , while $\vec{\Lambda}$ is the imaginary part of the PSP vector \vec{W} . In deriving the above equation of motion it is assumed that the input SOPs are the same for the entire wavelength. We propose a method that directly uses this equation of motion to measure the complex PSP vector \vec{W} . Eyal et al.[43] first noted this possibility; however they used four SOPs to estimate the complex PSP vector. We show that only three SOPs are sufficient to determine \vec{W} .

In addition, being an important component in optical systems, the fiber Bragg grating (FBG)'s PDL is also investigated in this part. A FBG can be used as a filter or as a sensor. It is comprised of an optical fiber with a periodic refractive index perturbation in the fiber core. It is made by exposure of the fiber to an intense UV interference pattern, created by either a split-beam interferometer or a phase mask. A PDL measurement of the FBG over the grating's reflection wavelength involves the use of an optical circulator. The optical circulator is a passive device having

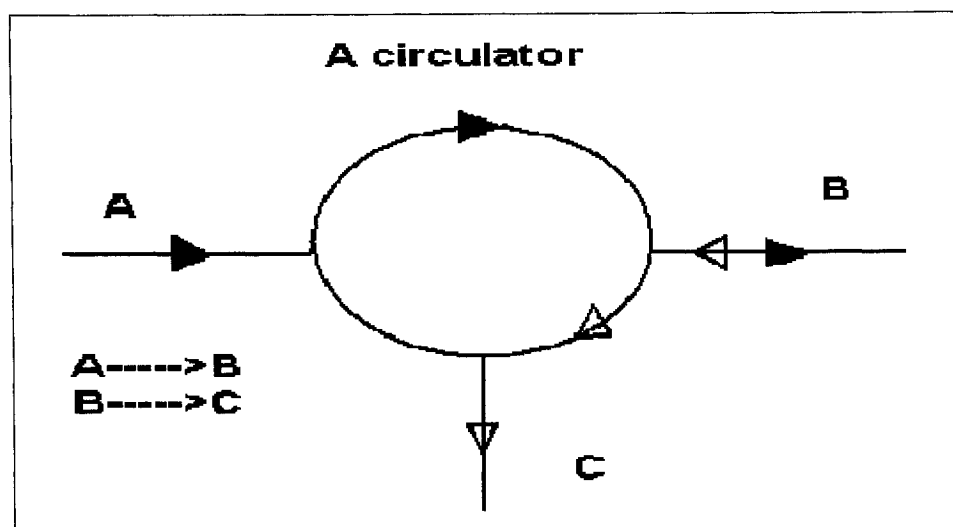


Figure 6.1: An optical circulator's function. The light comes from A goes to B, cannot go into C. The light comes from B goes to C, cannot go into A.

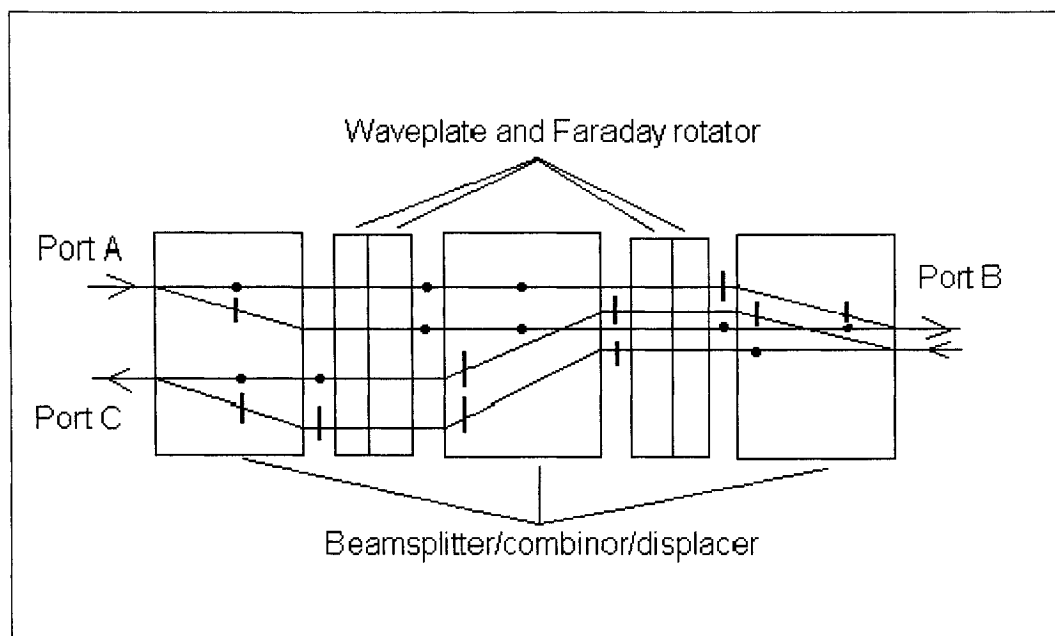


Figure 6.2: Working principle of an optical circulator. The dot and vertical line represent horizontal and vertical polarized beams, respectively.

three or more ports in which input light from one port is coupled only to the next sequential port in a given direction and is prevented from travelling in any other direction (Figure 6.1). The circulator is made up of beamsplitters (or called beam displacers, which separate the light beam into two perpendicularly polarized light beams: ordinary light and extraordinary light), waveplates (which provide +45 or -45 degree rotations depending on the direction of the input light) and Faraday rotators (Figure 6.2). By a combination of these components, the light from port A is separated into O beam and E beam, which pass through the components between port A and port B and are finally recombined into port B. But the light from port B will be separated, displaced and recombined into port C. It cannot go back to port A. As we can see, the circulator has many polarization dependent parts. The circulator has almost the same level of polarization dependent loss as the typical fiber optic device under test (DUT). In measurements, one usually ignores the circulator induced PDL since there is presently no method existing to eliminate it. In this work, there is proposed and demonstrated an experimental configuration and procedure, based on the Jones matrix method, to eliminate this PDL successfully in our measurement.

In the next three chapters, we will discuss the following polarization effects: 1) PMD measurement in an optical system, and 2) PDL measurement of a circulator.

CHAPTER 7

CHROMATIC DISPERSION AND POLARIZATION EFFECTS

7.1 The Physics of Polarization Effects

The refractive index n is dependent on light frequency ω , so one has the relation $n = n(\omega)$; this dependence is called chromatic dispersion (CD). Dispersion causes significant pulse broadening when a very short pulse propagates through a fiber, because a short pulse (in time domain) consists of more frequency components (obtained via Fourier transform) in spectral domain. These components have different velocities even in the same fiber dependent on the $n(\omega)$ function.

One defines the mode-propagation constant as [[8], page 9]:

$$\beta(\omega) = n(\omega)\frac{\omega}{c} = \beta_0 + \beta_1(\omega - \omega_0) + \frac{1}{2}\beta_2(\omega - \omega_0)^2 + \dots \quad (7.1)$$

where $\beta_m = (\frac{d^m\beta}{d\omega^m})_{\omega=\omega_0}$, ($m = 0,1,2,\dots$).

Next, if we refer to n_g as the group index and v_g as the group velocity, we have:

$$\beta_1 = \frac{1}{v_g} = \frac{n_g}{c} = \frac{1}{c}(n + \omega\frac{dn}{d\omega}) \quad (7.2)$$

Also the group-velocity dispersion (GVD) parameter is expressed as:

$$\beta_2 = \frac{d\beta_1}{d\omega} = \frac{1}{c}(2\frac{dn}{d\omega} + \omega\frac{d^2n}{d\omega^2}) \quad (7.3)$$

This is related to the commonly used dispersion parameter D :

$$D = \frac{d\beta}{d\lambda} = -\frac{2\pi c}{\lambda^2} \beta_2 \approx \frac{\lambda}{c} \frac{d^2 n}{d\lambda^2} \quad (7.4)$$

In standard fiber, when $\lambda = 1270$ nm, $\beta_2 = 0$ so $D = 0$ and we name this wavelength as λ_D , which is called the zero-dispersion wavelength. With different fiber manufacturing methods, we can shift this zero-dispersion wavelength to 1310 nm or even to 1550 nm, and even design dispersion-flattened fiber (with reduced wavelength dependence).

GVD severely limits the data transmission quality when the bit rate exceeds 2 Gb/s for existing telecommunication networks [[26], page 280] (which mostly use older, unmodified fiber). That is why dispersion management schemes are being investigated.

On the other hand, since two degenerate orthogonal modes are supported in a single mode fiber [[8], page 13], the mode propagation constants are different in the two polarization directions. If n_x and n_y are the modal refractive indices for x and y polarization states, then the modal birefringence is $B_m = |n_x - n_y|$, and the beat length is $L_B = \frac{\lambda}{B_m}$. In reality, all single mode fibers exhibit some modal birefringence because of unintentional variations in the core shape (asymmetries) and anisotropic stresses along the fiber length. PMD causes the broadening of the optical pulse because of random variations in the birefringence along the fiber, which is in addition to GVD induced pulse broadening. PMD limits the system performance when the single channel bit rate is extended to above 10 Gb/s [[26], page 280] and the use of dispersion management methods cannot completely eliminate

the PMD induced broadening. Some methods used to reduce the negative effects involve the use of electrical or optical delay lines to compensate for the first-order PMD [44] [45]. Higher order PMD compensation in a 40 Gb/s lightwave system has also being proposed [46] [47]. Also, polarization maintaining (PM) fibers, for example “Panda” and “Bow tie” designs are used to keep the polarization state fixed during transmission through the fiber for some applications.

Another polarization related parameter is the Polarization Dependent Loss (PDL), which is defined as the difference between the maximum and the minimum insertion losses for all possible input states of polarization (SOPs)[48].

7.2 Mathematical Description of Polarization

To begin, we review the definition originated by G. G. Stokes in the mid 19th century. He introduced 4 parameters to describe the polarization of light, which are now called Stokes parameters [[49], page 374].

$$S_0 = 2I_0 \tag{7.5}$$

$$S_1 = 2I_1 - 2I_0$$

$$S_2 = 2I_2 - 2I_0$$

$$S_3 = 2I_3 - 2I_0$$

where I_0, I_1, I_2 and I_3 are the transmitted intensities when each of 4 polarizers is inserted in the light path. These polarizers are isotropic, $+45^\circ$ linear, -45° linear and circular, respectively. And each of these filters will transmit half the incident

light, the other half being discarded. (S_0, S_1, S_2, S_3) is called Stokes vector. In the normalized representation $(1, 0, 0, 0)$ is the totally unpolarized light, $(1, 1, 0, 0)$ is horizontally polarized light and $(1, -1, 0, 0)$ is vertically polarized light. For completely polarized light, it follows that: $S_0^2 = S_1^2 + S_2^2 + S_3^2$. For partially polarized light, the degree of polarization (DOP) is defined as $V = (S_1^2 + S_2^2 + S_3^2)^{1/2} / S_0$.

R. C. Jones invented an alternate method to describe polarized light in the 1940s, called the Jones vector (or Jones Matrix) method [[49], page 376] which can be easily applied to coherent light if the phase information in the matrix is presented. The most important point is that the Jones matrix can be used to define the optical elements preserving phase information. Thus, light passing sequentially through a number of optical components represented by matrices A_1, A_2, A_3, \dots , can be described as $E_t = \dots A_3 A_2 A_1 E_i$. (E_i - initial amplitude, E_t - transmitted amplitude)

In 1943, H. Mueller devised a novel way to relate the Stokes method to the Jones matrix method. The Mueller matrix [[49], page 377], which is a 4×4 matrix, can be used to describe both polarized and partially polarized light, as well as coherent and non-coherent light.

The Stokes vector is defined as three dimensional vectors S_1, S_2 , and S_3 ; and moves on the surface of a sphere called the Poincare' sphere [Figure 7.1]. Points on the equator represent states of linear polarization, the poles represent right-hand (north pole) and left-hand (south pole) circular polarizations, and all other points on the sphere represent elliptical polarization states. If the device under test

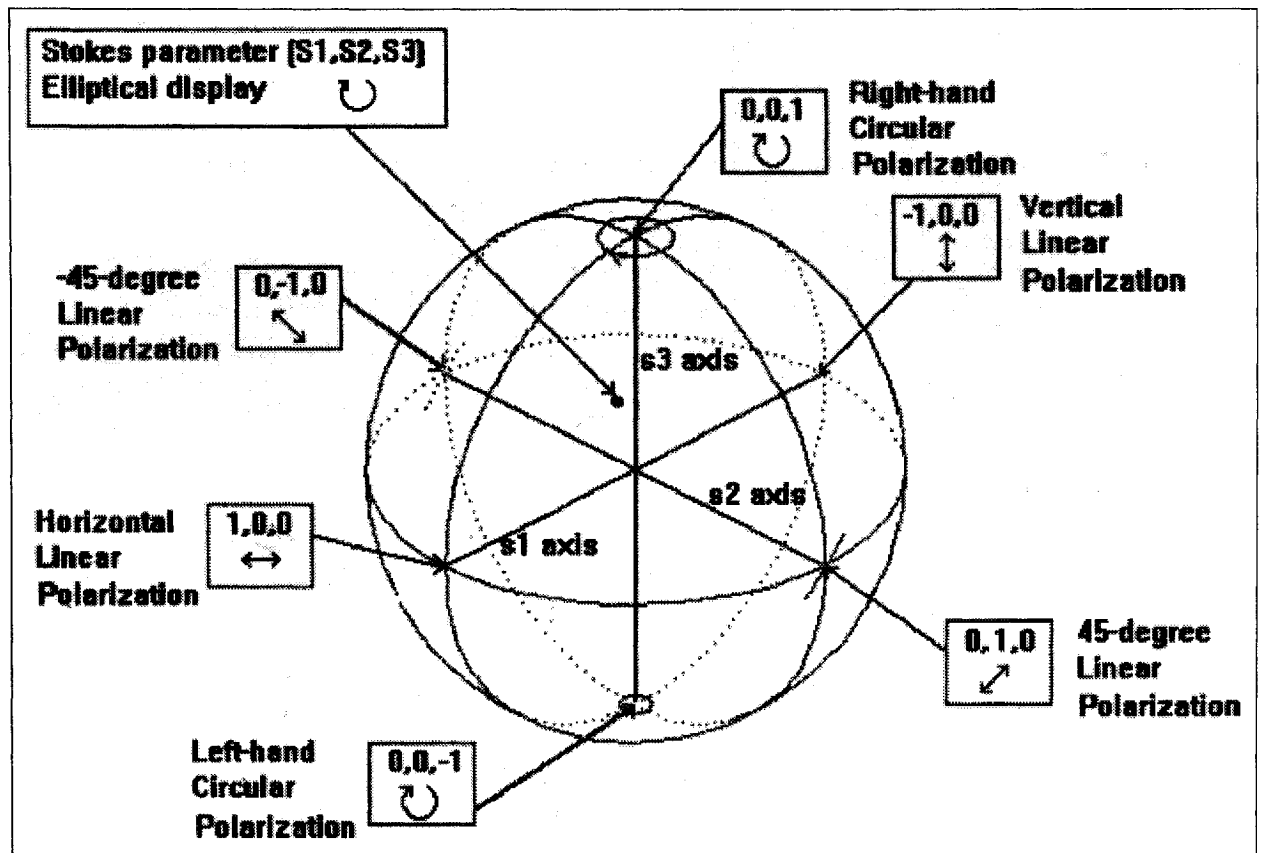


Figure 7.1: Polarization states can be described using an elliptical display, a point on the Poincaré sphere or a set of Stokes parameters [50].

is an optical component then as the wavelength changes, the component exhibits different birefringent characteristics, thus the polarization vector traces out a curve, or arc, on the surface of the Poincare sphere. The vector that goes from the center of the sphere to the circle represents the component's principal axis. For long fibers, i.e. fiber length L (say 5 km) \gg beat length (say 10 m), the PMD from fiber sections combines randomly, and thus the Stokes vector traces out a random curve that covers the Poincare sphere as the wavelength changes. The rate at which the vector to the curve changes divided by the rate at which the optical frequency changes, is defined as the PMD [35].

The relation between the Jones vector $(A_x \exp(i\phi_x), A_y \exp(i\phi_y))$ and Stokes vector (S_0, S_1, S_2, S_3) is given as [50]:

$$S_0 = A_x^2 + A_y^2 = 1 \quad (7.6)$$

$$S_1 = A_x^2 - A_y^2 = \cos(2\omega) \cos(2\alpha)$$

$$S_2 = 2A_x A_y \cos(\Delta) = \cos(2\omega) \sin(2\alpha)$$

$$S_3 = 2A_x A_y \sin(\Delta) = \sin(2\omega)$$

where $\vec{E} = iA_x \exp(i\phi_x) + jA_y \exp(i\phi_y)$, $\Delta = \phi_x - \phi_y$, α is the azimuth angle of the polarization ellipse and the ellipticity of the polarization ellipse is $\tan(\omega)$. For known input SOPs – 0° , 45° and 90° , the measured output SOPs are:

$$\begin{bmatrix} x_1 \\ y_1 \end{bmatrix}, \begin{bmatrix} x_2 \\ y_2 \end{bmatrix}, \begin{bmatrix} x_3 \\ y_3 \end{bmatrix} \quad (7.7)$$

If one defines $k_1 = x_1/y_1$, $k_2 = x_2/y_2$, $k_3 = x_3/y_3$, $k_4 = (k_3 - k_2)/(k_1 - k_3)$, then the corresponding Jones matrix is:

$$C \begin{bmatrix} k_1 k_4 & k_2 \\ k_4 & 1 \end{bmatrix} \quad (7.8)$$

where C is an unknown complex constant introduced by the Jones matrix measurement technique, this constant has no effect on the final PDL calculation.

Using Jones matrix eigenvalue analysis method, one can measure PMD and PDL [50].

For PMD measurement, one begins with measuring the Jones matrices J_1 and J_2 at preselected wavelengths λ_1 and λ_2 . The differential group delay (DGD), $\Delta\tau$, for these wavelengths is related to the eigenvalues ρ_1 and ρ_2 of the matrix product J_1 and J_2 . An eigenvalue is defined as a complex constant which satisfies the following relationship:

$$\rho \times V = J \times V$$

where J is the Jones matrix being analyzed, and V is the eigenvector input to J for which no polarization change occurs during signal transmission.

Thus we have [38]:

$$PMD_{1,2} = \text{Arg}(\rho_1/\rho_2)/(\omega_2 - \omega_1) \quad (7.9)$$

where Arg denotes the argument function.

For PDL measurement (as seen in Figure 7.2), we have [51]:

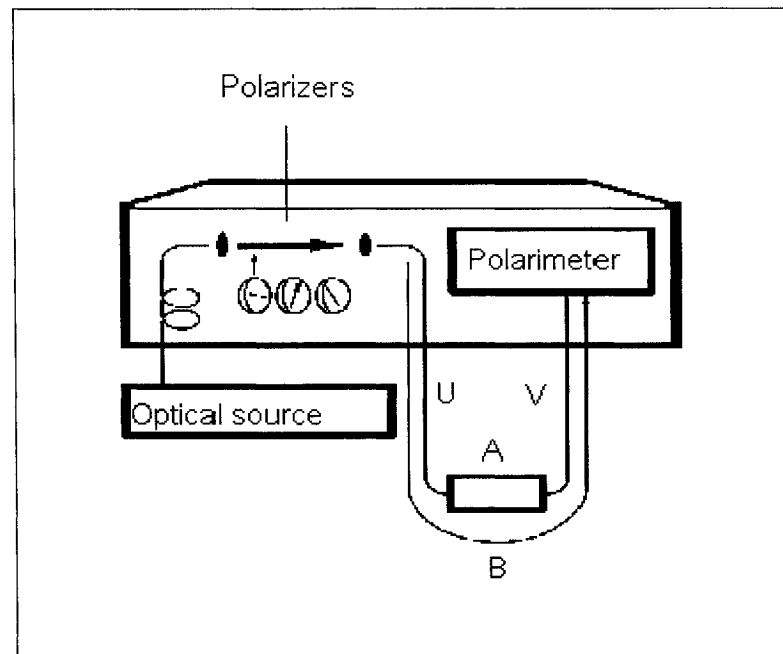


Figure 7.2: The Agilent 8509 Lightwave Measurement System. The PDL information is derived from the Jones matrix of the test component [50]. A , B , U , V represent the Jones matrices for the elements indicated (the component under test, one test fiber and the two leading fibers, respectively).

$$PDL = \frac{T_{\min}}{T_{\max}} = \frac{s_1^2(A)}{s_2^2(A)} = \frac{s_1^2(B)}{s_2^2(B)} \quad (7.10)$$

where A , B , U , V represent the Jones matrices for the elements indicated (the device under test and the three pigtailed), s is the singular value of the matrix, and T is the optical power transmission coefficient, 1 and 2 refer to two eigenvalues of the Hermitian matrix.

These mathematical descriptions are used in the following chapters to calculate PMD and PDL for the data measurements.

CHAPTER 8

POLARIZATION MODE DISPERSION AND POLARIZATION DEPENDENT LOSS MEASUREMENTS IN OPTICAL COMMUNICATION SYSTEMS

8.1 Equation of Motion

Before we describe the detailed measurement methods, we first discuss a few interesting facts regarding a combined PMD and PDL/G system. According to the PSP definition [35] [40], one can easily find the fast and slow state Stokes vectors from the condition:

$$\frac{d\vec{S}}{d\omega} = 0 \quad (8.1)$$

With the above conditions, the equation of motion is [42]:

$$\vec{\Omega} - \vec{\Lambda} \times \vec{S}_p = \lambda \vec{S}_p \quad (8.2)$$

where λ is a constant. One can solve the above equation to find the following solutions:

$$\left\{ \begin{array}{l} \vec{S}_p^\pm = \pm \left[\frac{\lambda}{\lambda^2 + \Lambda^2} \vec{\Omega} + \frac{(\vec{\Omega} \cdot \vec{\Lambda})}{\lambda(\lambda^2 + \Lambda^2)} \vec{\Lambda} \right] + \frac{1}{\lambda^2 + \Lambda^2} \vec{\Omega} \times \vec{\Lambda} \\ \lambda = \sqrt{\frac{1}{2} \left[\Omega^2 - \Lambda^2 + \sqrt{(\Omega^2 - \Lambda^2)^2 + 4 (\vec{\Omega} \cdot \vec{\Lambda})^2} \right]} \end{array} \right. \quad (8.3)$$

\vec{S}_p^+ and \vec{S}_p^- are not in general opposite to each other on the Poincaré sphere (i.e. they are not perpendicular in real space) unless

$$\vec{\Omega} \times \vec{\Lambda} = 0 \quad (8.4)$$

i.e. $\vec{\Omega}$ and $\vec{\Lambda}$ are parallel or anti-parallel with each other which is very unlikely. As a result, for a combined system with both PMD and PDL/G any time domain method measuring the maximum and minimum time delay to determine the DGD is not the same as the DGD between two PSPs, because one can never launch an input SOP completely in \vec{S}_p^+ or \vec{S}_p^- . Adopting the latter definition [40] [42], DGD is given by:

$$\tau_{DGD} = \text{Re} \left(\sqrt{\vec{W} \cdot \vec{W}} \right) \quad (8.5)$$

Closely associated with DGD is another new quantity:

$$\eta = \text{Im} \left(\sqrt{\vec{W} \cdot \vec{W}} \right) \quad (8.6)$$

which is called the differential attenuation slope (DAS) and these two terms are expressed explicitly as follows:

$$\tau_{DGD} = \lambda \quad (8.7)$$

$$\eta = \vec{\Omega} \cdot \vec{\Lambda} / \tau_{DGD} \quad (8.8)$$

η is related to PDL/G, but it is *not* equal to the true PDL/G of the system, because the corresponding output Stokes vectors for maximum and minimum loss/gain are always opposite with each other on the Poincaré sphere.

Similarly to the second-order PMD case, one can define second-order effects in the system with PDL/G. Here we introduce two second-order equations:

$$\begin{cases} \frac{d\vec{\Omega}}{d\omega} = \frac{d\Omega}{d\omega}\hat{\Omega} + \Omega\frac{d\hat{\Omega}}{d\omega} \\ \frac{d\vec{\Lambda}}{d\omega} = \frac{d\Lambda}{d\omega}\hat{\Lambda} + \Lambda\frac{d\hat{\Lambda}}{d\omega} \end{cases} \quad (8.9)$$

$\hat{\Omega}$ is a unit vector pointing in the direction of $\vec{\Omega}$, and $\hat{\Lambda}$ is a unit vector in the direction $\vec{\Lambda}$. Similar to the case of zero PDL/G [43], one can say the term $\frac{d\Omega}{d\omega}\hat{\Omega}$ describes a polarization dependent chromatic dispersion (PDCD) and the term $\Omega\frac{d\hat{\Omega}}{d\omega}$ describes the depolarization chromatic dispersion (DCD). Similarly, one calls the term $\frac{d\Lambda}{d\omega}\hat{\Lambda}$ the polarization dependent attenuation dispersion (PDAD) and the term $\Lambda\frac{d\hat{\Lambda}}{d\omega}$ the depolarization attenuation dispersion (DAD). All these second-order quantities can be calculated once the complex PSP vectors are obtained.

Next, we describe how to use the equations of motion to measure the real part of the PSP vector ($\vec{\Omega}$) and the imaginary part of the vector ($\vec{\Lambda}$). Considering the identity:

$$\vec{S} \cdot \frac{d\vec{S}}{d\omega} \equiv 0 \quad (8.10)$$

one immediately sees that the vector equation of motion gives two independent components. Therefore one needs to measure three different scans of the output SOPs as a function of angular frequency ω for three distinct input SOPs. Experimentally we can measure the three pairs of output Stokes vectors: $\vec{S}_1(\omega + \Delta\omega)$, $\vec{S}_1(\omega)$; $\vec{S}_2(\omega + \Delta\omega)$, $\vec{S}_2(\omega)$; and $\vec{S}_3(\omega + \Delta\omega)$, $\vec{S}_3(\omega)$. For the first measured pair we get:

$$\left\{ \begin{array}{l} \frac{d\vec{S}_1}{d\omega} \equiv \frac{d\vec{S}_1(\omega+\Delta\omega/2)}{d\omega} \approx \frac{\vec{S}(\omega+\Delta\omega)-\vec{S}_1(\omega)}{\Delta\omega} \\ \vec{S}_1 \equiv \vec{S}_1(\omega + \Delta\omega/2) \approx \frac{\vec{S}_1(\omega+\Delta\omega)+\vec{S}_1(\omega)}{|\vec{S}_1(\omega+\Delta\omega)+\vec{S}_1(\omega)|} \end{array} \right. \quad (8.11)$$

Repeating the same procedure for the second and third scan pairs; we have the following coupled equations at angular frequency $\omega + \Delta\omega/2$,

$$\left\{ \begin{array}{l} \frac{d\vec{S}_1}{d\omega} \equiv \vec{\Omega} \times \vec{S}_1 - (\vec{\Lambda} \times \vec{S}_1) \times \vec{S}_1 \\ \frac{d\vec{S}_2}{d\omega} \equiv \vec{\Omega} \times \vec{S}_2 - (\vec{\Lambda} \times \vec{S}_2) \times \vec{S}_2 \\ \frac{d\vec{S}_3}{d\omega} \equiv \vec{\Omega} \times \vec{S}_3 - (\vec{\Lambda} \times \vec{S}_3) \times \vec{S}_3 \end{array} \right. \quad (8.12)$$

For the real part of the PSP vector:

$$\left\{ \begin{array}{l} \vec{\Omega} \cdot (\vec{S}_1 + \vec{S}_2) = \frac{1}{1-\vec{S}_1 \cdot \vec{S}_2} \left(\frac{d\vec{S}_2}{d\omega} - \frac{d\vec{S}_1}{d\omega} \right) \cdot (\vec{S}_1 \times \vec{S}_2) \\ \vec{\Omega} \cdot (\vec{S}_2 + \vec{S}_3) = \frac{1}{1-\vec{S}_2 \cdot \vec{S}_3} \left(\frac{d\vec{S}_3}{d\omega} - \frac{d\vec{S}_2}{d\omega} \right) \cdot (\vec{S}_2 \times \vec{S}_3) \\ \vec{\Omega} \cdot (\vec{S}_1 + \vec{S}_3) = \frac{1}{1-\vec{S}_1 \cdot \vec{S}_3} \left(\frac{d\vec{S}_3}{d\omega} - \frac{d\vec{S}_1}{d\omega} \right) \cdot (\vec{S}_1 \times \vec{S}_3) \end{array} \right. \quad (8.13)$$

For the imaginary part of the PSP vector:

$$\left\{ \begin{array}{l} \vec{\Lambda} \cdot (\vec{S}_1 + \vec{S}_2) = \frac{1}{1-\vec{S}_1 \cdot \vec{S}_2} \left(\vec{S}_1 \cdot \frac{d\vec{S}_2}{d\omega} + \vec{S}_2 \cdot \frac{d\vec{S}_1}{d\omega} \right) \\ \vec{\Lambda} \cdot (\vec{S}_2 + \vec{S}_3) = \frac{1}{1-\vec{S}_2 \cdot \vec{S}_3} \left(\vec{S}_2 \cdot \frac{d\vec{S}_3}{d\omega} + \vec{S}_3 \cdot \frac{d\vec{S}_2}{d\omega} \right) \\ \vec{\Lambda} \cdot (\vec{S}_1 + \vec{S}_3) = \frac{1}{1-\vec{S}_1 \cdot \vec{S}_3} \left(\vec{S}_1 \cdot \frac{d\vec{S}_3}{d\omega} + \vec{S}_3 \cdot \frac{d\vec{S}_1}{d\omega} \right) \end{array} \right. \quad (8.14)$$

One can solve the above coupled linear equations to obtain the quantities $\vec{\Omega}$ and $\vec{\Lambda}$. To have a unique solution, then \vec{S}_1 , \vec{S}_2 and \vec{S}_3 must be non-coplanar. This can be arranged in the experimental setup.

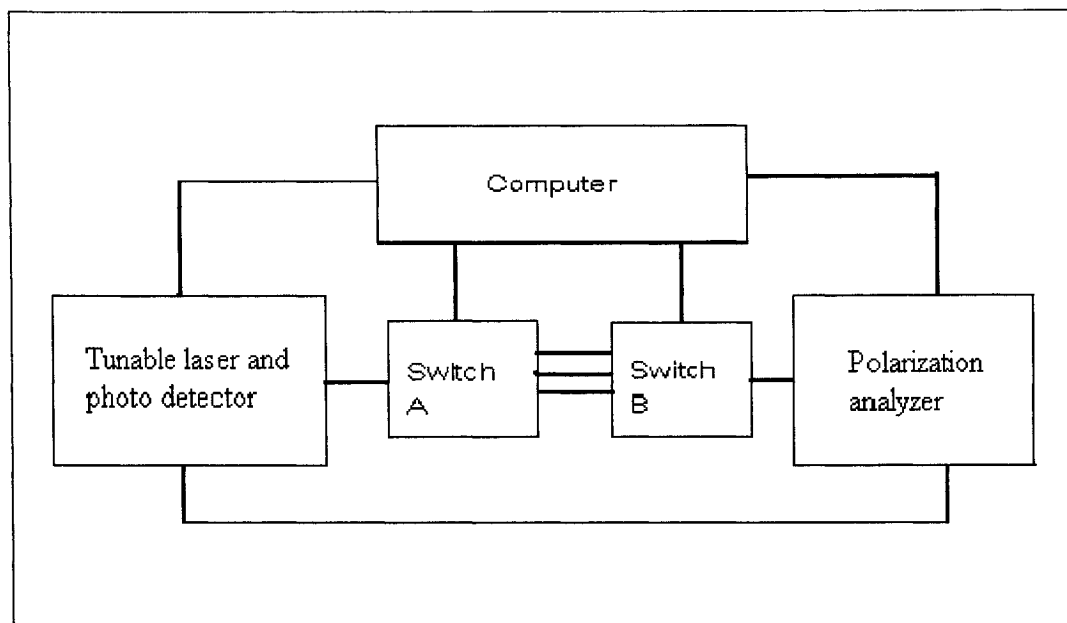


Figure 8.1: The test setup for PMD measurements. The computer controls the two optical switches simultaneously. 3 lines between the two switches represent 3 states of polarization.

8.2 Experimental Results

We have constructed test equipment based on this new algorithm. Figure 8.1 shows a schematic diagram of the experimental setup; it consists of a HP8164A light wave measurement system (including a tunable laser and a photo detector), two JDS Uniphase Corporation's optical switches (SB and SC models) for polarization control and a HP8509B polarization analyzer.

We have measured DGD [See Figure 8.2] for a fixed EXFO EM550 PMD emulator using both the HP8509B polarization analyzer and our own test setup as shown in Figure 8.1, and obtained excellent agreement. In Figure 8.3, we show

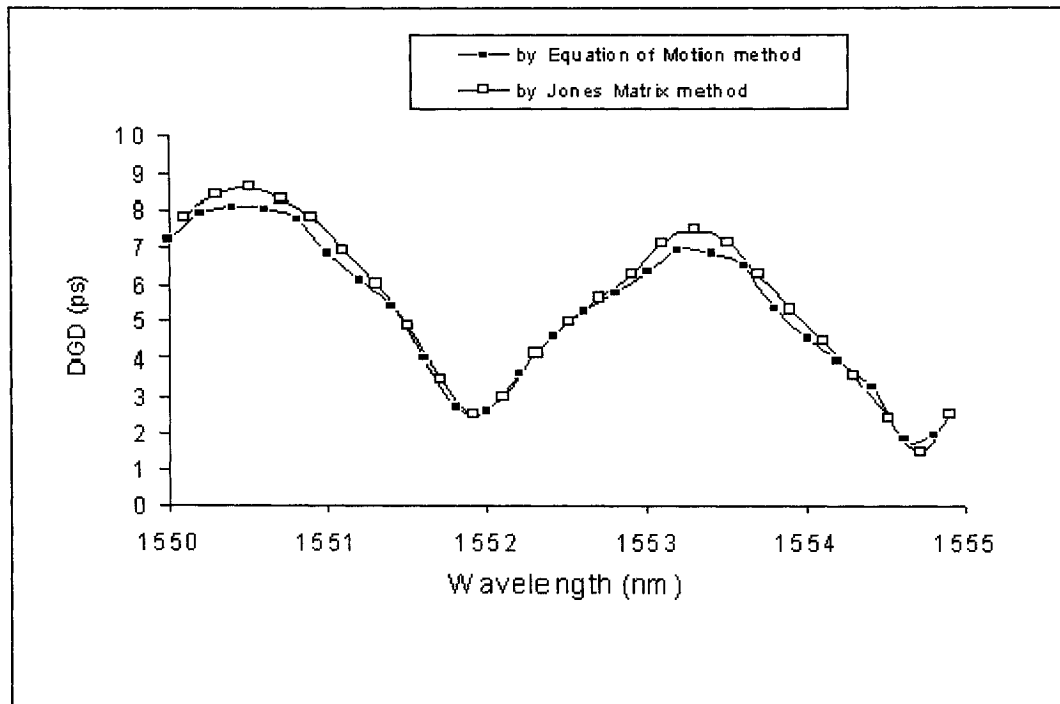


Figure 8.2: A comparison of DGD measurements using Jones Matrix eigen-value analysis and the new experimental method.

the PDL of the same emulator and in Figure 8.4, we plotted the corresponding DAS (differential attenuation slope). The setup is very simple and gives a direct measurement of the spectrally resolved complex PSP vector. The measurement speed is limited by the tuning speed of the measurement laser.

Polarization effects are important, not only in optical systems, but also in individual optical components. In the next chapter, this thesis will discuss the measurement of PDL in fiber Bragg gratings.

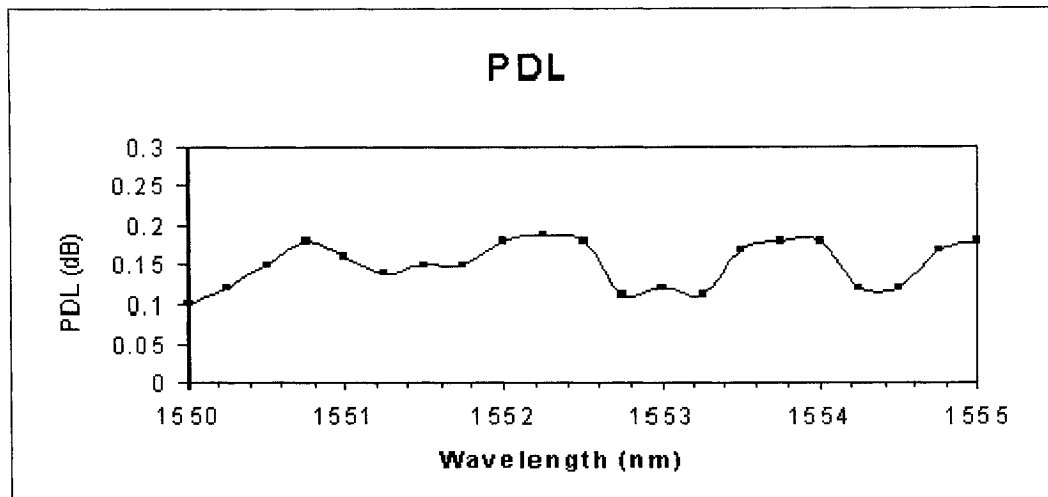


Figure 8.3: PDL test result for the PDL emulator. As we can see, it is not the same with the DAS test result in the following figure..

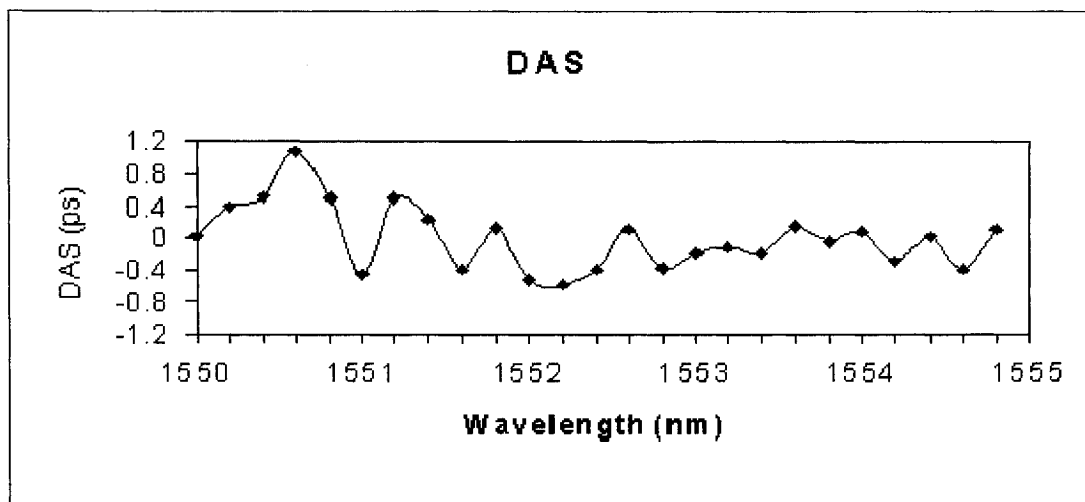


Figure 8.4: The differential attenuation slope (DAS) for the same emulator.

CHAPTER 9
MEASUREMENT OF POLARIZATION DEPENDENT LOSS IN FIBER
BRAGG GRATINGS

9.1 The Physics of Fiber Bragg Gratings

The fiber Bragg grating (FBG) was invented by Dr. Hill in the 1970s at Communication Research Canada (CRC), thus it is also called the Hill grating. The FBG can be used as both a filter and as a sensor.

A fiber Bragg grating has a periodic structure (refractive index perturbation) which is formed in the core of an optical fiber by exposure to an intense UV interference pattern. The grating can be made by using a split-beam interferometer or a phase mask to form the fringes.

As shown in Figure 9.1, the Bragg condition is [[52], page 96]:

$$\lambda_B = 2n_{eff}\Lambda \quad (9.1)$$

where the Bragg grating wavelength, λ_B , is the free space center wavelength of the input light that will be back-reflected from the Bragg grating, Λ is the spatial period of the index modulation, and n_{eff} is the effective refractive index of the fiber core at the free space center wavelength. The Bragg grating resonance, which is the center wavelength of the back-reflected light from the Bragg grating depends on the effective index of refraction of the core and the periodicity of the grating.

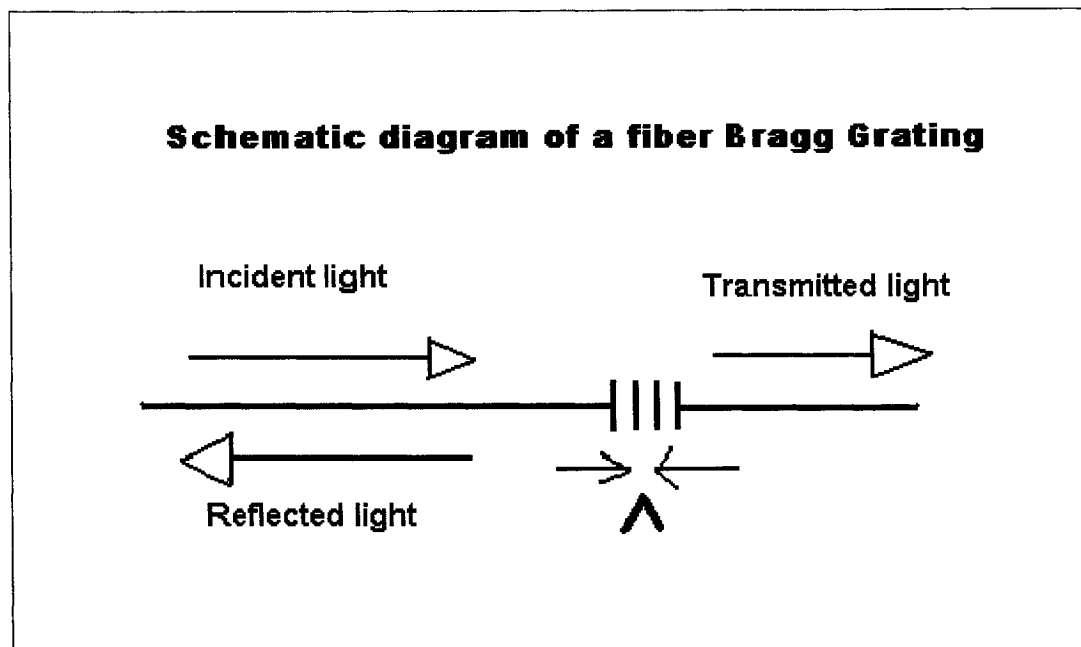


Figure 9.1: A FBG.

The effective index of refraction, as well as the periodic spacing between the grating peaks will be affected by changes in strain and temperature. Thus, the FBG can be used as a sensor as well as a filter.

9.2 PDL and PMD Measurement of FBG

With the development of higher speed and more complicated fiber optic networks, more components, such as circulators and FBGs, are now widely used. Most components have both PDL and PMD [53]. The PDL and PMD characterization of components is critical for system design and evaluation because both PDL and PMD limit the data capacity of high-speed fiber optic communication systems. Two major methods for measuring PDL, the polarization scanning method (PSM)

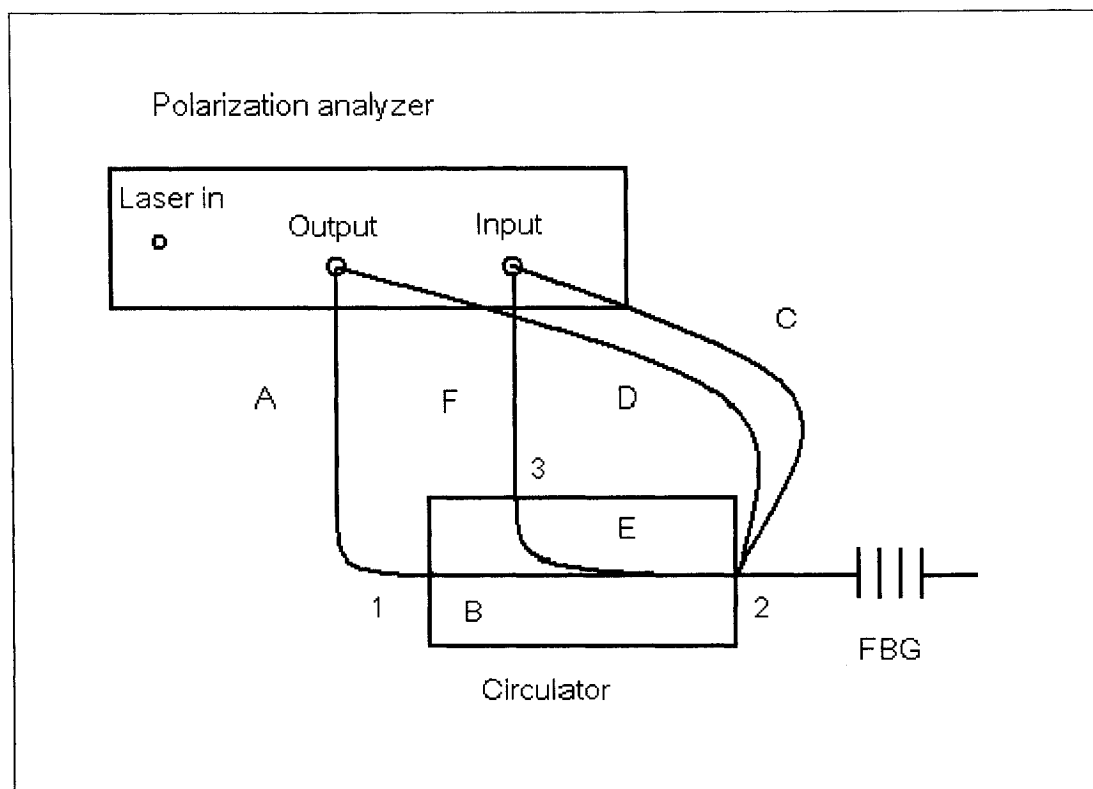


Figure 9.2: The configuration for measuring PMD and PDL of a FBG.

and the Jones Matrix Eigenvalue analysis (JME) method have been reported [48]. However, there is no commercially available test method that can characterize the reflection PDL of a FBG because the circulator (or the coupler) has to be used for the reflection measurement and the circulator has the same level of PDL that the FBG has. The PDL value measured by current methods is actually the effective PDL of the combination of the FBG and the circulator (or coupler). The PDL of the FBG itself is still unknown. Here we have proposed a method that can measure the PDL and PMD of the FBG (on reflection) and eliminate the PDL influence of the circulator.

Figure 9.2 gives a block diagram of the PDL and PMD measurement for a FBG. The method is similar to the JME method, but three steps are involved. For a frequency ω , three Jones matrices are measured. Port refers to the port of the circulator, while Output and Input refer to the output and input of the polarization analyzer. The three measurement steps are as follows:

1) The Jones matrix, T_1 , for the link Output \rightarrow Port 1 \rightarrow Port 2 \rightarrow Input is measured. T_1 can be written as $T_1 = CBA$, where A is the Jones matrix of the fiber cable from Output to Port 1, B is the Jones matrix from Port 1 to Port 2 and C is the Jones matrix of the fiber cable from Port 2 to Input.

2) The Jones matrix, T_2 , for the link Output \rightarrow Port 2 \rightarrow Port 3 \rightarrow Input is measured and can be written as: $T_2 = FED$, where F is the Jones matrix of the fiber cable from Port 3 to Input, E is the Jones matrix from Port 2 to Port 3, and D is the Jones matrix from Port 2 to Output.

3) The Jones matrix, T_3 , for the link Output \rightarrow Port 1 \rightarrow Port 2 \rightarrow FBG \rightarrow Port 3 \rightarrow Input is measured and can be written as $T_3 = FEGBA$.

Knowing the three Jones matrices T_1, T_2 and T_3 , the PDL and PMD of the FBG can be calculated.

Consider the Jones matrix T

$$T = T_2^{-1}T_3T_1^{-1} = D^{-1}E^{-1}F^{-1}FEGBAA^{-1}B^{-1}C^{-1} = D^{-1}GC^{-1} \quad (9.2)$$

If the same cable from Port 2 to the Input and Output is used, then $D^{-1} = C$ and Equation 9.2 can be rewritten as:

$$T = CGC^{-1} \quad (9.3)$$

The PDL of the FBG is [48]:

$$PDL = 10 \cdot \log_{10} \left(\frac{\lambda_1}{\lambda_2} \right)$$

where λ_1 and λ_2 are the two eigenvalues of G^+G ; they are the same eigenvalues of T^+T because C is a unitary rotation matrix. T^+ denotes the complex conjugate transpose of the matrix T .

Using similar analysis, the DGD of the FBG can be expressed as [38]:

$$\Delta\tau = \frac{[\text{Arg}(\rho_1/\rho_2)]}{\Delta\omega} \quad (9.4)$$

where ρ_1 and ρ_2 are the two eigenvalues of $T(\omega + \Delta\omega)T^{-1}(\omega)$ and Arg denotes the argument function (i.e. phase angle).

The tunable laser used for this experiment is the HP 8164A, the polarization analyzer used is the HP 8509B, and the circulator is the JDS Uniphase Corporation's model CR 5500. Both the tunable laser and polarization analyzer are controlled with a PC (via a LabView program) through the GPIB bus. The data is processed and presented using Matlab v6.5.

The FBG used here is made at CRC with a 0.7 nm spectral range (Bragg wavelength) from 1550.8 nm to 1551.5 nm. Because the maximum PMD of a circulator is typically 0.05 ps [54], compared to 1 - 10 ps for the PMD of a FBG, we may assume that the new method won't cause obvious error in the PMD measurement

when using a normal JME method.

In order to compare the different results using our new method with those using the normal JME method for the same FBG, Figures 9.3 and 9.4 show the PDL measurements results. Keeping the circulator position fixed, measurements are undertaken when the connector of the FBG is rotated by 0, 60 and 140 degrees respectively. Figure 9.3 shows the PDL test before eliminating the effect from the circulator. The maximum uncertainty is around 0.15 dB which is almost the same as the PDL for a conventional circulator. This means the measurement is incorrect when one does not consider the PDL of the circulator. Figure 9.4 shows the PDL test result after using the new measurement method to eliminate the effect of the circulator. The maximum uncertainty is reduced to 0.05 dB. Comparing these two graphs, it is clear that the new measurement method characterizes the PDL of the FBG more accurately.

Note that there are still some uncertainties involved in the new method. For instance the optical connector used in the experiment has a PDL typically less than 0.05 dB but could have some impact, this error could be eliminated by splicing fibers (reducing loss 0.00 dB with perfect splicing).

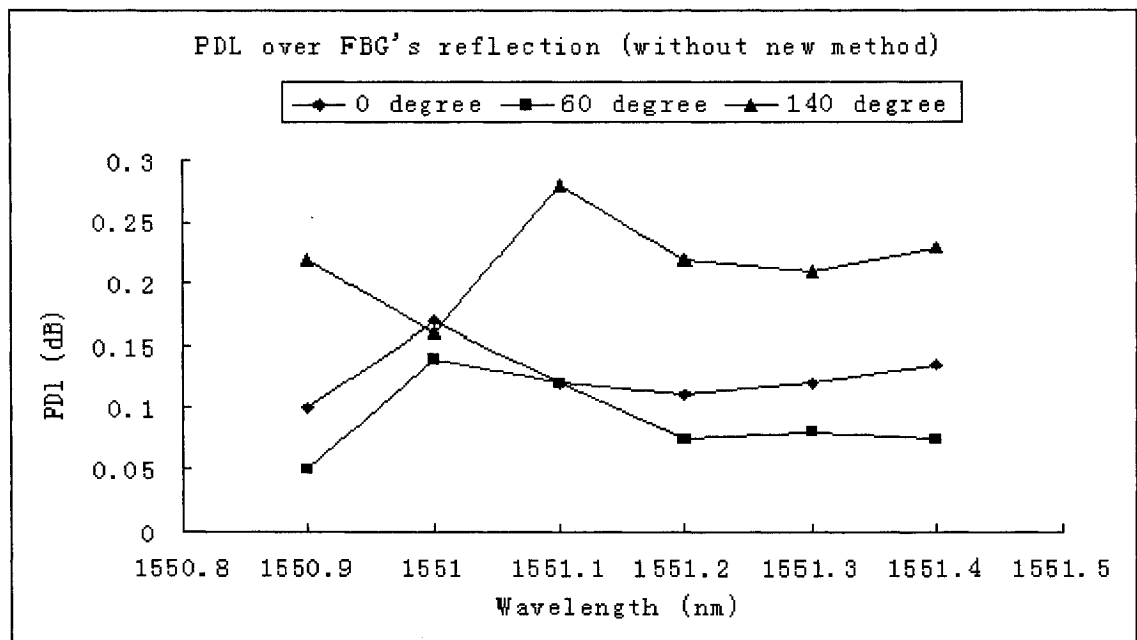


Figure 9.3: PDL measurements before using new approach. The PDL values are between 0.05 to 0.3 dB.

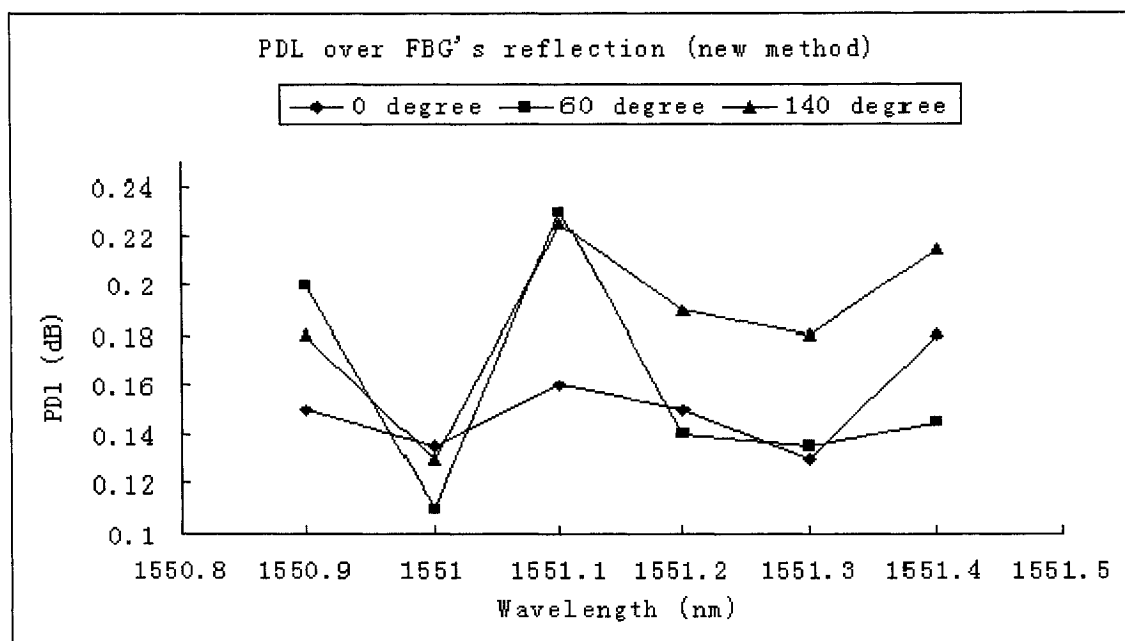


Figure 9.4: PDL measurements using new approach. The PDL values are between 0.1 to 0.24 dB.

CHAPTER 10

SUMMARY (PART II)

In this section of the thesis, research on polarization effects has been performed. In this field, PMD and PDL effects in an optical communication system and fiber Bragg grating have been studied. An algorithm and experimental setup to test the FBG reflection PDL has been proposed which can eliminate the effects of the circulators; also an algorithm was proposed and a test set was built to measure the PMD in a PDL and PMD combined system. This reduced the test requirement from 4 SOP measurements to 3 SOP measurements by using a complex PSP vector calculation. Note also that the fiber Bragg gratings can be used as strain and temperature sensors, similarly to the ordinary optical fibers being used as strain and temperature sensors through the Brillouin scattering effect. Also it should be pointed out here that the biggest difference between these two sensors is that the Brillouin scattering sensor is a distributed sensor while the FBG sensor is a single point sensor. In the future, I hope to continue to contribute to advancing these sensors.

A. ABBREVIATIONS

AOM	Acoustic-Optical Modulator
B-OTDA	Brillouin scattering based Optical Time Domain Analysis
CFRP	Carbon Fiber Reinforced Plastic
CW	Continuous Wave
DAS	Differential Attenuation Slope
DFB	Distributed Feedback
DGD	Differential Group Delay
DWDM	Dense Wavelength Division Multiplexing
EOM	Electro-Optic Modulation
FBG	Fiber Bragg Grating
FC/PC	Fiber Connection/Physical Contact
FC/APC	Fiber Connection/Angled Fiber Connection
FWHM	Full Width at Half Maximum
GVD	Group-Velocity Dispersion
JME	Jones matrix Eigenvalue
LD	Laser Diode
OA	Operational Amplifier
OTDR	Optical Time Domain Reflectometer
PDL/G	Polarization Dependent Loss/Gain
PI	Proportional Integrator
PMD	Polarization Mode Dispersion

PSP	Principal State of Polarization
Nd:YAG	Neodymium-Yttrium-Aluminium Garnet-Laser
SNR	Signal to Noise Ratio
SOP	State of Polarization

B. LIST OF SYMBOLS

ω	optical angular frequency
ν	optical frequency
λ	wavelength
ϵ_0	electric permittivity of vacuum
χ	susceptibility
n	refractive index
α	fiber loss
I_S	Stokes intensity
I_p	pump intensity
g_B	Brillouin gain coefficient
g_p	peak value of Brillouin gain
T_B	phonon lifetime
Γ_B	damping rate
v_A	acoustic velocity
k	wave vector
T	temperature
ϵ	strain
C_T	temperature-frequency coefficient
C_ϵ	strain-frequency coefficient
G	transfer function
A_{eff}	effective core area

L_{eff}	effective interaction length
\vec{E}	electrical vector
\vec{P}	polarization vector
\vec{W}	principal state of polarization vector
\vec{S}	normalized Stokes vector
β	mode-propagation constant
D	dispersion parameter
n_g	group index
v_g	group velocity
B_m	modal birefringence
L_B	beat length
V	degree of polarization
τ_{DGD}	differential group delay
η	differential attenuation slope
λ_B	Bragg grating wavelength
Λ	spatial period of the index modulation
n_{eff}	effective refractive index

C. THE SIMULATION CODE FOR BRILLOUIN SENSOR WITH BROADSPECTRAL linewidth BY MATLAB 6.5

```
%% file name- c://MATLAB6P5/work/chen5MHz.m %%  
  
clear;  
  
format long;  
  
gP=5e-11;  
  
BeatFreq=10860;  
  
DampRate=100;  
  
alpha=0.0461e-3;  
  
deltaz=1;  
  
deltafreq=0.005;  
  
FWHM=5;  
  
%% set parameters %%  
  
freq1=10820;  
  
freq2=10900;  
  
fiberlength=20;  
  
numberoftrial=20;  
  
U=1e3;  
  
%% start to calculate %%  
  
Ipinitial=0.020/(pi*(5e-6)^2);%Ip(1)  
  
Isinitial=0.001/(pi*(5e-6)^2);%Is(fiberlength)  
  
c1=gP*(DampRate/2)^2;
```

```

c2=(DampRate/2)^2;

c3=(sqrt(pi)*log(4)/1e3)^2;

c4=-4*log(2);

for x2=freq1:freq2;

x2

Ip(1)=Ipinitial;

Ip1(1)=Ipinitial;

Is(1)=Ipinitial;

Is1(1)=Isinitial;

for num=1:numberoftrial;

for m=1:fiberlength-1;

sum1(m)=0;

sum2(m)=0;

for ni=1:1000;

for nj=1:1000;

temp1=c1/((x2+(ni+nj)*deltafreq-BeatFreq)^2+c2)*c3*exp(c4*((0.5-ni/1000)^2+(0.5-
nj/1000)^2));

sum1(m)=sum1(m)+Ip(m)*Is(m)*temp1;

sum2(m)=sum2(m)+Ip1(m)*Is1(m)*temp1;

end

end

Ip(m+1)=-alpha*Ip(m)-sum1(m)+Ip(m);

```

```

Is(m+1)=alpha*Is(m)-sum1(m)+Is(m);

Ip1(m+1)=-alpha*Ip1(m)-sum2(m)+Ip1(m);

Is1(m+1)=alpha*Is1(m)-sum2(m)+Is1(m);

end

if ((Is(fiberlength)+Is1(fiberlength))/2)>Isinitial;

Is(1)=(Is(1)+Is1(1))/2;

else

Is1(1)=(Is(1)+Is1(1))/2;

end

if abs((Is(fiberlength)+Is1(fiberlength))/2-Isinitial)<U;

break

end

end

%% plot results %%

if x2==BeatFreq;

subplot(2,2,1), plot(Is);

xlabel('Fiber Position (m)');

ylabel('Is (W/m*m)');

string1={'Stokes Signal along the Fiber'};

title(string1);

subplot(2,2,2), plot(Ip);

xlabel('Fiber Position (m)');

```

```

ylabel('Ip (W/m*m)');

string2={'Pump Signal along the Fiber'};

title(string2);

else

end

y2(x2-freq1+1)=Ipinitial-Ip(fiberlength/2);

end

x1=freq1:freq2;

y1=gP*(DampRate/2)^2./((x1-BeatFreq).^2+(DampRate/2)^2);

subplot(2,2,3), plot(y1);

xlabel('Beat Frequency - 10820 (MHz)');

ylabel('gB (m/W)');

string3={'Theoretical gB Profile'};

title(string3);

subplot(2,2,4), plot(y2);

xlabel('Beat Frequency - 10820 (MHz)');

ylabel('Ip(z=0)-Ip(z=10m) (W/m*m)');

string4={'Brillouin Spectrum at 10m along the Fiber'};

title(string4);

%% the end %%

```

D. CURRICULUM VITAE

Ou Chen, Bachelor of Engineering, Optical Engineering, Beijing Institute of Technology. 1986-1990.

Since then, the author worked at the Academic Institute of China, Chinetek Group and also at 3M, JDS Uniphase and OZ Optics as an electro-optical technician and engineer.

The author started the Master of Science study at the University of Ottawa in October 2001 .

E. PAPERS, POSTERS AND PRESENTATIONS

- “Polarization mode dispersion measurement in a system with polarization dependent loss or gain”, L. Chen, O. Chen, S. Hadjifaradji, X. Bao, IEEE Photonics Technology Letters, Vol.16, No.1, January 2004.
- “Automated measurements of PDL and PMD over fiber Bragg grating’s reflection wavelength”, Ou Chen, Ping Lu, Liang Chen, and Xiaoyi Bao, PRO (photonics research Ontario), Niagara Falls, 2002.
- “Frequency stabilized 1550nm lasers for distributed fiber optic Brillouin sensor systems”, Ou Chen, Lufan Zou, Guilin Wu, Dan Falk, John Bernard, Xiaoyi Bao, Liang Chen, ISIS (intelligent sensing for innovative structures) Canada, Vancouver 2003.
- “Development of the offset locking based distributed sensor”, Ou Chen, Yidun Wan, Lufan Zou, Xiaoyi Bao, Liang Chen, Photonics North, Ottawa 2004.

REFERENCES

- [1] Tsuneo Horiguchi, Toshio Kurashima and Mitsuhiro Tateda, "Tensile strain dependence of Brillouin frequency shift in Silica optical fibers", *IEEE Photonics Technology Letters*, Vol. 1, No. 5, May 1989.
- [2] Anthony Wayne Brown, Ph.D thesis, "Development of a Brillouin scattering based distributed fiber optic strain sensor", Physics Department, University of New Brunswick, 2000.
- [3] Massimo Facchini, Ph.D thesis, "Distributed optical fibre sensors based on Brillouin scattering", Laboratoire de Metrologie, Ecole Polytechnique Federale de Lausanne.
- [4] X. Bao, D. J. Webb, and D. A. Jackson, "22-km distributed temperature sensor using Brillouin gain in an optical fiber", *Optics Letters*, Vol. 18, No.7, pp. 552-554 (1993).
- [5] Yoshiyuki Doi, Seiji Fukushima, Tetsuichiro Ohno, and Kaoru Yoshino, "Frequency stabilization of millimeter-wave sub-carrier using laser heterodyne source and optical delay line", *IEEE Photonics Technology Letters*, Vol. 13, No. 9, Sept. 2001.
- [6] Amnon Yariv, "Optical electronics in modern communication", fifth edition, California Institute of Technology, Oxford University Press, ISBN: 0-19-510626-1.
- [7] Graham Ferrier, M.Sc thesis, "Spectral characterization of distributed Brillouin sensors in the transient regime", Physics Department, University of Ottawa, 2003.
- [8] Govind P. Agrawal, "Nonlinear fiber optics", third edition, the Institute of Optics, University of Rochester, Optics and Photonics, Academic Press, ISBN: 0-12-045143-3.
- [9] Technical Note, "Electrostriction", Encyclopaedia Britannica Article, Encyclopaedia Britannica, Inc.
- [10] R. G. Smith, "Optical power handling capacity of low loss optical fibres as determined by stimulated Raman and Brillouin scattering", *Applied Optics*, 11, 2489, 1972.

- [11] Product Note, "SMF-28 CPC6 single-mode optical fiber product information", Corning Inc..
- [12] J. Smith, M.Sc. thesis, "Characterization of the Brillouin loss spectrum for simultaneous distributed sensing of strain and temperature", University of New Brunswick, 1999.
- [13] M. O. van Deventer and A. J. Boot, "Polarization properties of stimulated Brillouin scattering in single-mode fibers", *J. Lightwave Technology* 12, 585 (1994).
- [14] Toshio Kurashima, Tsuneo Horiguchi, and Mitsuhiro Tatedda, "Thermal effects on the Brillouin frequency shift in jacketed optical fibers", 20 May 1990, Vol. 29, No. 15, *Applied Optics*.
- [15] Lufan Zou, Xiaoyi Bao, Shahraam Afshar V., and Liang Chen, "Dependence of the Brillouin frequency shift on strain and temperature in a photonic crystal fiber", *Optics Letters*, Vol. 29, No. 13, July 2004.
- [16] X. Bao, D. J. Webb, and D. A. Jackson, "32-km distributed temperature sensor based on Brillouin loss in an optical fiber", *Optics Letters*, Vol. 18, No. 18, pp. 1561-1563 (1993).
- [17] Lufan Zou, Xiaoyi Bao, Yidun Wan, and Liang Chen, "Coherent probe-pump based Brillouin sensor for centimeter crack detection", submitted to *Optics Letters*.
- [18] X. Zeng, Q. Yu, G. Ferrier, X. Bao, R. E. Steffen, and M. Bowman, "Strain measurement of the load test on the Rollinsford bridge using the distributed Brillouin sensor", 1st Intl. Workshop on Structure Health Monitoring of Innovative Civil Engineering Structure, 2002.
- [19] Z. Liu, G. Ferrier, X. Bao, X. Zeng, Q. Yu, A. Kim, "Brillouin scattering based distributed fiber optic temperature sensing for fire detection", 7th Intl. Symposium on Fire Safety Science, Worcester, Massachusetts, USA, June 2002.
- [20] L. Zou, G. A. Ferrier, S. Afshar V., Q. Yu, L. Chen and X. Bao, "Distributed Brillouin scattering sensor for discrimination of wall thinning defects in steel pipe under internal pressure", *Applied Optics*, Vol. 43, No. 7, March 2004.
- [21] Y. Etem, M. F. Lewis, and P. Sample, "An optical microwave source for frequency synthesizer applications", Intl. Topical Meeting Microwave Photon., 1996, paper WE1-5, pp. 161-164.
- [22] R. T. Ramos and A. J. Seeds, "Fast heterodyne optical phase-lock loop using double quantum well laser diodes", *Electron. Lett.*, Vol. 28, pp. 82-83, 1992.

- [23] R. P. Braun, G. Grosskopf, D. Rohde, and F. Schmidt, "Low-phase noise millimeter-wave generation at 64 GHz and data transmission using optical sideband injection locking", *IEEE Photonics Technology Letter*, Vol. 10, pp. 728-730, 1998.
- [24] Toshiaki Suhara, "Semiconductor Laser Fundamentals", Osaka University, Marcel Dekker, Inc., ISBN: 0-8247-5373-9.
- [25] Product Note, "Semiconductor Laser Diodes - SPECIFICATIONS", NTT Electronics Corporation.
- [26] Govind P. Agrawal, "Fiber-optic communication systems", third edition, Wiley Interscience, ISBN: 0-471-21571-6, 2002.
- [27] Stephan R. Kurtz, "Mixers as phase detectors", Tech-notes, WJ Communications, Inc.
- [28] Bert C. Henderson, "Mixers in microwave systems (Part 1)", Tech-notes, WJ Communications, Inc.
- [29] Technical Note, "Fiber Optic Components - Optical Amplifiers & External Modulators - Theory of Operation - Lithium Niobate Amplitude and Phase Modulators", Force, Incorporated.
- [30] W. K. Burns, R. P. Moeller, C. H. Bulmer, and A. S. Greenblatt, "Depolarized source for fiber-optic applications", *Optics Letters*, Vol. 16, No. 6, pp. 381-383, 1991.
- [31] Steve Yao, Yongqiang Shi, and Jianwei Ma, "Scrambling to reduce polarization-related impairments", Technical Note, General Photonics Corporation.
- [32] Product Note, "125 Specifications", Lightwave Electronics.
- [33] X. Bao, J. Dhliwayo, N. Heron, D. Wedd and D. A. Jackson, "Experimental and theoretical studies on a distributed temperature sensor based on Brillouin scattering", *J. of Lightwave Technol.* Vol. 13, No. 7, July 1995.
- [34] L. Chen and X. Bao, "Analytical and numerical solutions for steady state stimulated Brillouin scattering in a single-mode fiber", *Opt. Commun.* 152, 65 (1998).
- [35] C. D. Poole and R. E. Wagner, "Phenomenological approach to polarization dispersion in long single mode fibers", *Electron. Lett.*, Vol. 22, No. 19, pp. 1029-1030, 1986.
- [36] C. D. Poole, N. S. Bergano, R. E. Wagner, and H. J. Schulte, "Polarization dispersion and principal states in 147 km undersea lightwave cable", *J. Lightwave Technology*, Vol. 6, pp. 1185-1988, July 1988.

- [37] P. A. Williams and C. M. Wang, "Corrections to fixed analyzer measurements of polarization mode dispersion", *J. Lightwave Technology*, Vol. 16, pp. 534-541, April 1998.
- [38] B. L. Heffner, "Automated measurement of polarization mode dispersion using Jones matrix eigen-analysis", *IEEE Photon. Technology Lett.*, Vol. 4, No. 9, Sept. 1992.
- [39] A. Eyal, M. Tur, "Measurement of polarization mode dispersion in systems having polarization dependent loss or gain", *IEEE Photon. Technology Lett.*, Vol. 9, pp. 1256-1258, Sept. 1997.
- [40] N. Gisin and B. Huttner, "Combined effects of polarization mode dispersion and polarization dependent losses in optical fibers", *Optics Commun.*, Vol. 142, pp. 119-125, Oct. 1997.
- [41] N. J. Frigo, "A generalized geometrical representation of coupled mode theory", *IEEE J. Quantum Electron.*, QE-22, pp. 2131-2140, Nov. 1986.
- [42] Y. Li and A. Yariv, "Solutions to the dynamic equation of polarization-mode dispersion and polarization-dependent losses", *J. Opt. Soc. Am. B*, Vol. 17, pp. 1821-1827 Nov. 2000.
- [43] A. Eyal, M. Tur, "A modified Poincare sphere technique for the determination of polarization mode dispersion in the presence of differential loss/gain", *Proc. OFC'98*, pp. 340.
- [44] B. W. Hakki, "Polarization mode dispersion compensation by phase diversity detection", *IEEE Photonics Technology Letter* 9, 121, 1997.
- [45] L. Moller, "Filter synthesis for broad-band PMD compensation in WDM systems", *IEEE Photonics Technology Letter* 12, 1258 (2000).
- [46] M. Shtaif, A. Mecozzi, M. Tur, and J. Nagel, "A compensator for the effects of high-order polarization mode dispersion in optical fibers", *IEEE Photonics Technology Letter*, 12, 434 (2000).
- [47] Q. Yu, L. S. Yan, Y. Xie, M. Hauer, and A. E. Willner, "Higher order polarization mode dispersion compensation using a fixed time delay followed by a variable time delay", *IEEE Photonics Technology Letter* 13, 863, 2001.
- [48] Ping Lu, Liang Chen, and Xiaoyi Bao, "Statistical distribution of polarization-dependent loss in the presence of polarization-mode dispersion in single-mode fibers", *IEEE Photonics Technology Letters*, Vol. 13, 451-453, May 2001.
- [49] Eugene Hecht, "Optics", 4th edition, Adelphi University, Addison Wesley, ISBN: 0-8053-8566-5.

- [50] Product Note, "Polarization measurements of signals and components", Agilent 8509B/C lightwave polarization analyzers, Product note 8509-1, Agilent Technologies.
- [51] B. L. Heffner, "Deterministic, analytically complete measurement of polarization-dependent transmission through optical devices", IEEE Photon. Technology Lett., Vol. 4, No. 5, May 1992.
- [52] Andreas Othonos, "Fiber Bragg gratings: fundamentals and applications in telecommunications and sensing", Kyriacos Kallim, Boston, Mass., Artech House, 1999. TA1800.084.
- [53] N. Gisin, B. Huttner, "Combined effects of polarization mode dispersion and polarization dependent loss in optical fibers", Optical Communications, Vol. 142, 119-125 (1997).
- [54] Product Note, "Polarization-insensitive circulator", Product bulletin, JDS Uniphase Corporation.